

Large eddy simulation of spilling and plunging breakers

Erik Damgaard Christensen

DHI Water & Environment (DHI), Agern Allé 5, DK-2970 Hørsholm, Denmark

Received 6 April 2004; received in revised form 3 June 2005; accepted 24 November 2005

Available online 10 January 2006

Abstract

A Navier–Stokes solver with a free surface model is used for simulating wave breaking, undertow, and turbulence in breaking waves. The free surface model is based on the Volume of Fluid concept. Turbulence scales larger than the grid scale are simulated directly while turbulence scales smaller than the grid scale are represented by a sub-grid scale model. Two different approaches for the sub-grid scale model have been applied, which are the Smagorinsky model and a model based on a k -equation for the sub-grid scale turbulence. The waves approach the shore in shore-normal direction and break on a plane constant sloping beach. Periodic spilling and plunging breakers are simulated for 20 and 16 wave periods, respectively. The set-up, undertow, and turbulence levels are compared to experimental results. Despite the rather coarse resolution of the computational domain, satisfactory results for the wave height decay and undertow have been obtained. However, the turbulence levels are over-predicted when using the standard values of the model parameters and a complete answer to this problem has not been found. Furthermore, the evolution of vorticity over the wave period has been studied. It shows that at the initial breaking point vorticity is generated around the vertical as well as around the transverse axis. Later vorticity around the longitudinal axis (offshore–onshore direction) is generated, probably through deformation of vorticity around the other axis.

© 2005 Elsevier B.V. All rights reserved.

Keywords: Breaking waves; Undertow; Flow structures; Numerical models; Large eddy simulation

1. Introduction

The study of surf zone dynamics has been subject to extensive research during the last few decades. The following papers give a good introduction to the subject: [Peregrine \(1983\)](#), [Battjes \(1988\)](#), and [Svendsen and Putrevu \(1996\)](#). [Christensen et al. \(2002\)](#) give a review of the latest research of the flow structures across the surf zone, [Longo et al. \(2002\)](#) review the research on turbulence in the surf zone, and [Elfrink and Baldock \(2002\)](#) focus on the swash zone dynamics.

One of the early optical measuring techniques, LDV, has been used widely for the surf zone breaking wave investigations. [Stive \(1980\)](#) was among the first, if not the first, to apply the LDV technique to measure the internal flow field under periodic breaking waves. [Nadaoka and Kondoh \(1982\)](#) presented LDV measurements for the internal velocity field within the surf zone. [Nadaoka et al.](#)

[\(1989\)](#) used the LDV technique to study the structures of turbulent flow field of spilling breakers in the surf zone. One of the recent comprehensive studies on turbulence transport under surf zone breaking waves using LDA technique was that of [Ting and Kirby \(1994, 1995, 1996\)](#). The turbulence transport was studied in detail by determining each term in the k -equation. Interesting results were reported especially on the different mechanisms between different types of breaking waves. The cross-shore sediment transport, which is associated with the correlation between the mean and turbulent flow, was found from simple reasoning to be offshore under spilling breakers but onshore under plunging breakers.

Experimental investigations of the aerated region in the upper part of breaking waves cannot use optical measuring techniques as air bubbles too often corrupt the optical signal. Therefore other techniques are employed as in [Jansen \(1986\)](#) and more recently [Lin and Hwung \(1992\)](#). They used a flow visualisation technique with the use of ultraviolet light to illuminate fluorescent tracer particles, which were fed into the air bubble region. Their photographic and video images

E-mail address: edc@dhi.dk.

revealed a well-known sequence of jet-splash motions in both plunging and spilling breakers. In Jansen's (1986) results, smooth trajectories of the particles inside the jet-splash motions suggested so-called coherent motions in the flow. In Lin and Hwung's (1992) results, the main mechanism that drives the motion in the bubble zone was found to be the vortex system that was generated from the jet-splash cycles. Vortex stretching was also found to occur due to the interaction between the jets, the vortices, and the effect of the rising buoyant bubbles. These effects are perhaps the main causes of the development of the obliquely descending eddies observed by Nadaoka et al. (1988) and Nadaoka et al. (1989). In the field experiments eddies were found to involve large amounts of air bubbles which enhanced the upwelling of sediment. Due to scale effects the amount of entrained air is relatively larger in large waves (field experiments) compared to small waves (laboratory experiments).

The most direct way to investigate the flow in the surf zone numerically is to solve the basic equations for Newtonian fluids, called the Navier–Stokes equations. In many other areas than coastal hydrodynamics, such as aerodynamics and fluid mechanics, the method has gained much attention during the last few decades evolving into a whole discipline called Computational Fluid Dynamics (CFD). The method is capable of calculating the flow in complex geometries to give very refined information about velocities, turbulence, transport properties, etc.

A highly recognised method for free surface flow is the marker and cell method, which was invented by Harlow and Welch (1965). It is based on markers that are distributed all over the fluid domain. Each marker follows the velocity field in a Lagrangian way. An example of the MAC method used for breaking waves is given in Sakai et al. (1986). A similar method to the MAC method is the surface markers method presented by Chen et al. (1991) and used for breaking waves in Christensen and Deigaard (2001). Here the markers are only situated at the surface, which reduces the computational costs and improves the accuracy.

The above methods find the position of the surface in a Lagrangian manner. Another approach that has been widely used during recent years is based on a continuity equation for a conservative quantity F that is solved in a Eulerian way. A straightforward way to solve the problem is to use a very accurate higher order convection scheme such as QUICK, used by Kawamura and Miyata (1994). In their case both the air and fluid flow were simulated around ships and submerged bodies. In Hirt and Nichols (1981) a special advection scheme was used to avoid smearing of the surface, which they called the "Volume of Fluid", also known as VOF. This method has been extensively used, modified, and improved by several researchers. The approach described in Ubbink (1997) is used in this work.

An early attempt to model flow and turbulence in the surf zone was undertaken by Lemos (1992). He applied the original VOF method invented by Hirt and Nichols (1981) together with a k - ε -model to represent the turbulence scales

in the simulations. The results showed that the approach could be used for simulating surf zone turbulence, though turbulence levels were over-predicted. Lin and Liu (1998a,b) used a similar approach to Lemos (1992), but with a further developed code of Hirt and Nichols (1981) by Kothe et al. (1991). Again the k - ε -model was used for representing the turbulence scales. As in Lemos (1992), Lin and Liu (1998a,b) found that the turbulence levels at breaking were overestimated. The error was of the order of 2 to 3 times the measured quantity. In the inner zone the turbulence is in general 25% to 50% higher than measured in Ting and Kirby (1994). A similar approach as the one sketched above was used in Lin and Liu (1998b) to investigate the turbulence transport and vorticity dynamics in the surf zone under plunging breakers. Compared to the results of a spilling breaker the results for the plunging breaker case compare better with measurements with respect to the undertow. The turbulence levels are too high just after the breaking point but closer to the shoreline the turbulence levels seem to be of the same order of magnitude as in the experiments by Ting and Kirby (1995). Bradford (2000) made a comparative study of three turbulence models. All three turbulence models used the turbulent viscosity concept combined with different formulations of the k - ε model. In general the model like k - ε -model and k -model gave an average turbulence level that was twice as large as the experimental levels reported by Ting and Kirby (1994) for the spilling breaker, while the RNG-model gave slightly smaller overestimations. The turbulence levels were found to be very close to the measured ones in the case of a plunging breaker, which agreed well with the results shown in Lin and Liu (1998a). The undertow found by both Bradford (2000) and Lin and Liu (1998a) was in general too low or directed towards the shore instead of offshore in the spilling breaker, which perhaps indicates that a periodic solution had not been found yet.

Even though Lin and Liu (1998a,b) used a more advanced description of the Reynolds stresses than Bradford (2000), their formulation did not show substantial improvements over the isotropic models. The choice of the boundary conditions, grid resolution, and the model coefficients all seem to have more impact on the solution. Mayer and Madsen (2000) found that the traditional turbulence models never find a stationary level of turbulence and eddy viscosity. The problem arises due to stability problems in the k - ω model in wave driven orbital motion. In Zhao et al. (2000) a multi-scale turbulence model is set-up based on a k - l model. Since the production term is still related to the strain rate the waves produce turbulence before they actual have broken. The instability reported by Mayer and Madsen (2000) was avoided, and therefore the simulated water elevations agreed well with measurements. Recently, Emarat et al. (2000) studied the mechanics of a surf zone plunging breaker. Results from 2D PIV measurements were compared against those from a numerical model based on the Navier–Stokes equations and the VOF method. Good agreement between both results was found for the comparison of the flow field

and velocity magnitude distribution. This study actually shows that the main problem in modelling the surf zone with Navier–Stokes solvers is the turbulence and perhaps the effect of air and the dynamics.

Large eddy simulation (LES) is another way of simulating turbulence in wave breaking, with turbulence model for the sub-grid turbulence only. Since it is a smaller part of the turbulence regime the model has to take account for, the model can be much simpler than the models used in Reynolds Averaged Navier–Stokes equation (RANS). Two-dimensional modelling cannot be said to be true LES, since the simulation of eddies is only two-dimensional, therefore the stretching of eddies that is characteristic for true turbulence is not simulated at all. However, the work of Zhao and Tanimoto (1998) shows a surprisingly good comparison with measurements of the vertical distribution of for instance the maximum and minimum orbital velocities. The wave height and mean water level distribution also compared well with measurements. Despite the defects of only two dimensions and that the slope of the submerged reef was 1:2, the model surely gave some good indications of the strength of an LES model. This work was continued in Zhao et al. (2004), where the multi-scale turbulence model was used to simulate breaking waves that were compared to Ting and Kirby (1994, 1995, 1996). Again a better agreement of the wave set-up is found. Further, the modelling of the undertow is improved; however, the shape of the undertow profile does not seem to follow the measured profiles in all cases. This was recognised by the authors who argued that the measurements had stronger mixing perhaps from air bubbles. The reason for these discrepancies is a matter of discussion. For instance a full three-dimensional flow field will change the mixing and therefore also the undertow profiles no matter how good a turbulence model is. No direct comparisons of turbulence levels were made to the measurements by Ting and Kirby (1994, 1995, 1996). This would have been a valuable contribution to the discussion of the mixing. It is clear that Zhao et al. (2004) predict wave set-up and the overall continuity better than found in previous studies. This might be explained by the fact that they avoid the stability mechanism described in Mayer and Madsen (2000), when using the multi-scale model.

Christensen and Deigaard (2001) used a full three-dimensional Navier–Stokes solver combined with a two-dimensional free-surface model based on the surface markers method to study the three-dimensional turbulent flow structures in the breaking zone. A Smagorinsky sub-grid model, Smagorinsky (1963), was used for the simulations. Watanabe and Saeki (1999) found similar results from three-dimensional simulations of breaking waves. The coherent flow structures were generated almost instantly at the breaker point and were enhanced by the breaking process. Finally, the flow structures broke down outside the region affected by the surface roller. The processes of growth of vorticity around vertical and transverse axis were further discussed in Watanabe et al. (2000). Watanabe and Saeki (2002) studied the velocity field after wave breaking.

The present study concerns numerical simulation of spilling and plunging breakers. The model is a full three-dimensional model solving the Navier–Stokes equations. The free surface model is based on the Volume of Fluid concept. In contrast to the study in Christensen and Deigaard (2001) the free surface is fully three-dimensional. Further, the problem with mass-conservation has been minimised by introducing another free surface method based on Volume of Fluid (VOF). The solver is based on a non-orthogonal curvilinear finite volume solver instead of the Cartesian finite difference solver used in Christensen and Deigaard. Introducing these changes made it possible to make comparisons to the time averaged quantities of undertow and turbulence in Ting and Kirby (1994).

The turbulence scales larger than the grid scale are simulated directly, Large Eddy Simulation (LES), while the effect of the smaller turbulence scales is represented by a sub-grid scale model. Two sub-grid scale models are tested. The first is the Smagorinsky model and the second is a sub-grid model based on a k -equation. The wave parameters and geometry resemble the physical experiments reported in Ting and Kirby (1994). This provides a rather comprehensive comparison between numerical and experimental results in order to provide validation of the use of LES for studying breaking waves.

2. The numerical model

The Navier–Stokes equations consist of a continuity equation and a momentum equation as sketched below:

Continuity equation:

$$\frac{\partial u_i}{\partial x_i} = 0 \quad (1)$$

Momentum equations:

$$\rho \frac{\partial u_i}{\partial t} + \rho u_j \frac{\partial u_i}{\partial x_j} = - \frac{\partial p}{\partial x_i} + \frac{\partial}{\partial x_j} \mu \left(\frac{\partial u_i}{\partial x_j} + \frac{\partial u_j}{\partial x_i} \right) \quad (2)$$

where ρ is the density of the fluid, u_i is the velocity components, p is the pressure, μ is the dynamical viscosity, and t and x are the time and spatial independent variables.

For small Reynolds numbers the Navier–Stokes equations can be solved directly without a turbulence model. This approach is called Direct Numerical Simulation (DNS), as it does not include a turbulence model. It is only small-scale flows that can be solved by DNS such as a wave boundary layer for small Reynolds numbers. Another approach is Large Eddy Simulation (LES), which is quite similar to DNS, the difference being that only the larger eddies are directly simulated, while the smaller scale eddies, i.e. smaller than the grid scale, are accounted for through a sub-grid scale model. In general DNS and LES require a fine resolution in three spatial dimensions, thus the CPU-time for such calculations is rather excessive and therefore the practical engineering applications can be limited with today's computers.

2.1. The sub-grid model for large eddy simulation

The basis for the Large Eddy Simulation is the spatial filtering of the Navier–Stokes equations. Using a top-hat filter the grid can be used as the filter itself. This is the most common way of filtering when the solution method is based on the finite volume method. The velocity scales smaller than the grid can naturally not be simulated anyway. The following equation summarizes the filtering process for the momentum equation:

$$\rho \frac{\partial \bar{u}_i}{\partial t} + \rho \frac{\partial \overline{u_i u_j}}{\partial x_j} = -\frac{\partial \bar{p}}{\partial x_i} + \frac{\partial}{\partial x_j} \mu \left(\frac{\partial \bar{u}_i}{\partial x_j} + \frac{\partial \bar{u}_j}{\partial x_i} \right) \quad (3)$$

In Eq. (3) the second term on the left-hand side has to be split up in a part that can be simulated directly:

$$\frac{\partial \overline{u_i u_j}}{\partial x_j} = \frac{\partial \bar{u}_i \bar{u}_j}{\partial x_j} + \left(\frac{\partial (\overline{u_i u_j} - \bar{u}_i \bar{u}_j)}{\partial x_j} \right). \quad (4)$$

The first part is simulated directly while the second part is moved to the right-hand side and has to be modelled. This part is also called the sub-grid scale Reynolds stress:

$$\tau_{ij}^s = -\rho (\overline{u_i u_j} - \bar{u}_i \bar{u}_j). \quad (5)$$

Eq. (5) is the closure problem for which we have to use a model. If no model is applied resolved turbulent kinetic energy can only dissipate due to the physical viscosity and the artificial numerical viscosity. This will often lead to a too slow dissipation of energy giving too high turbulence levels. Furthermore, the artificial numerical dissipation depends on the resolution, the numerical discretation, the algorithm and is normally not known, which adds uncertainty to the solution. Therefore a clear definition of how the excess energy should be dissipated is important even in cases where the turbulence is not of main interest.

2.1.1. Smagorinsky sub-grid model

A number of different sub-grid scale models (sgs models) have been proposed. Many of these are based on the Smagorinsky sgs model. This is an eddy viscosity model that is closely connected to the strain rate and the grid size. The sub-grid scale stresses:

$$\tau_{ij}^s = -\rho (\overline{u_i u_j} - \bar{u}_i \bar{u}_j) \quad (6)$$

are modelled in the following way:

$$\tau_{ij}^s - \frac{1}{3} \tau_{kk}^s \delta_{ij} = 2\mu_t \bar{S}_{ij}, \quad (7)$$

$$\bar{S}_{ij} = \frac{1}{2} \left(\frac{\partial \bar{u}_i}{\partial x_j} + \frac{\partial \bar{u}_j}{\partial x_i} \right).$$

The eddy viscosity is found according to:

$$\mu_t = \rho (C_s \Delta)^2 |\bar{S}| \quad (8)$$

where Δ is the filter length scale and $|\bar{S}| = (2\bar{S}_{ij}\bar{S}_{ij})^{1/2}$. C_s is the Smagorinsky constant that is in the order of 0.065 to 0.2. The model is rather simple which is an advantage in the computation. However, the optimal value of the Smagorinsky constant varies from flow to flow. For instance close to a wall the Smagorinsky constant can be reduced according to the van Driest damping.

2.1.2. *k*-equation sub-grid model

The sub-grid scale stresses:

$$\tau_{ij}^s = -\rho (\overline{u_i u_j} - \bar{u}_i \bar{u}_j) \quad (9)$$

are modelled based on a *k*-equation for the sub-grid scale turbulence:

$$k_{sgs} = -\frac{1}{2} (\overline{u_i u_i} - \bar{u}_i \bar{u}_i) \quad (10)$$

$$\frac{\partial k_{sgs}}{\partial t} + \bar{u}_j \frac{\partial k_{sgs}}{\partial x_j} = -\frac{1}{\rho} \tau_{ij} \frac{\partial \bar{u}_i}{\partial x_j} - C_\epsilon k_{sgs}^{3/2} + \frac{\partial}{\partial x_j} \left((\nu + \nu_t / \sigma_k) \frac{\partial k_{sgs}}{\partial x_j} \right) \quad (11)$$

The eddy viscosity is found according to:

$$\nu_t = \rho C_k \sqrt{k_{sgs}} \Delta \quad (12)$$

From this the sub-grid scale stresses can be found using a viscosity concept as follows:

$$\tau_{ij}^s - \frac{1}{3} \tau_{kk}^s \delta_{ij} = 2\rho \nu_t \bar{S}_{ij}, \quad (13)$$

$$\bar{S}_{ij} = \frac{1}{2} \left(\frac{\partial \bar{u}_i}{\partial x_j} + \frac{\partial \bar{u}_j}{\partial x_i} \right)$$

C_k is a coefficient, which in homogeneous, isotropic turbulence has been found to be in the order of 0.05 to 0.065, Yoshizawa (1986) and Menon et al. (1996). In Kim and Menon (1999) a dynamic version of the model estimated the coefficient close to a wall as:

$$C_k = 0.055 \left[1 - \exp\left(- (y^+)^2 / (A^+)^2\right) \right] \quad (14)$$

The term in brackets is similar to a van Driest damping, but the coefficient is damped even more close to the bed compared to the van Driest profile. The dissipation coefficients, C_ϵ and σ_k , are set equal 1 according to Menon et al. (1996).

2.1.3. Dynamic models

A rather successful extension of the model is the dynamic model. Here a test filter is introduced where the sub-grid stresses on each grid level and an optimal choice of C_s can be elaborated. Additional averaging of the method is

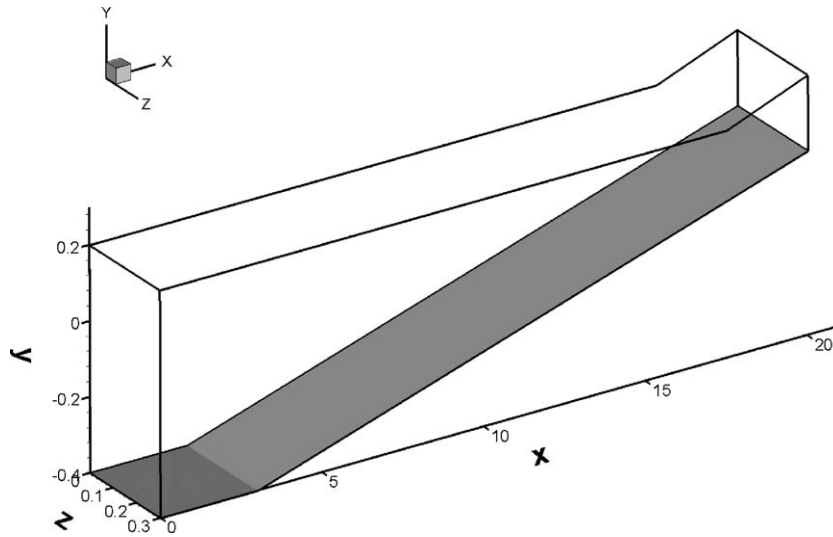


Fig. 1. The computational domain. The slope is 1:35 and the depth is 0.4 m. The width is 0.3 m.

needed due to large variation in the preliminary estimate of C_s . In a channel flow the quantities are averaged in the longitudinal and transverse directions. Due to the necessity of averaging in one or more directions the method cannot be used for general complicated flows, like for instance the simulation of the flow over a submerged structure in the surf zone.

2.2. Numerical algorithm

The solution of the Navier–Stokes equations is based on the finite volume method for general non-orthogonal mesh. The basic solver was described in Mayer et al. (1998), later extended to include the VOF method and several turbulence models. The solver was used to study green water incidents on ships in Nielsen and Mayer (2004). The spatial discretation is given in the Appendix and the algorithm is outlined in the following.

The velocity at the ‘inlet’ boundary where the waves are generated is specified according to the 5th order Stokes theory or 5th order Cnoidal theory. A general method as a stream function theory could have been used, but at the beginning of the study the two wave theories were already implemented and sufficient for this study.

2.2.1. The algorithm

The solution procedure is based on the fractional step method, which is a higher order time integration scheme. The procedure in the method used here is based on an explicit time stepping. This gives some limitations by the CFL criteria, but the use of the VOF method to track the free surface implies similar restrictions on the time step.

The algorithm is:

1. Move the surface by the VOF method (see the next section)

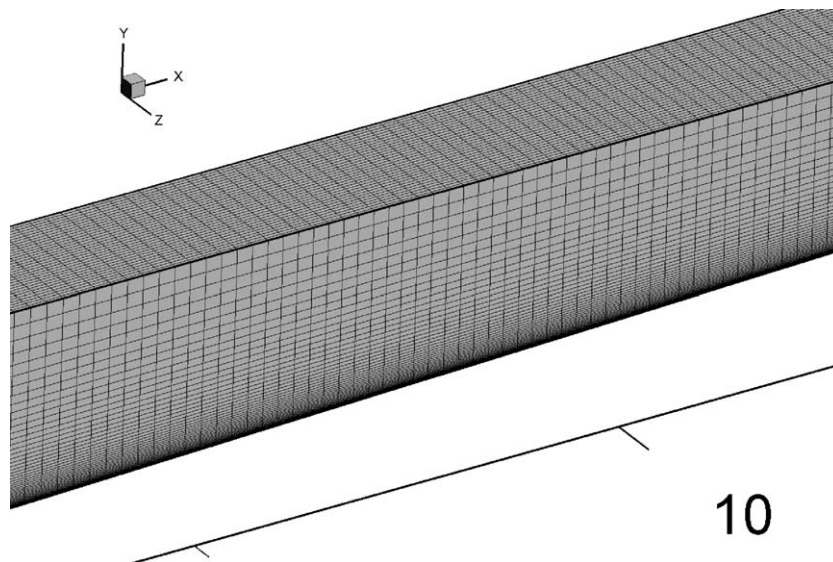


Fig. 2. The curvilinear grid consists of $320 \times 48 \times 32$ cells. It is stretched towards the bed and towards the area breaking.

Table 1
Wave parameters for the simulations

Breaker type	H_0 (m)	H_b (m)	T (s)	H_0/L_0	ξ_0	x_b (m)	d_b (m)
Spilling	0.127	0.125	2.0	0.020	0.20	10.1	0.196
Plunging	0.089	0.128	5.0	0.0023	0.60	11.495	0.156

2. The tentative velocity u^* field is found from the fractional step method
3. The velocity correction potential ϕ is found
4. The corrected velocity and fluxes are found
5. The pressure is found and the right-hand side for u^*

Step 1 and the modifications of the spatial scheme due to the free surface are treated in Section 2.3.

The tentative velocity u^* is found from the following equation (step 2):

$$\frac{\text{Vol} \cdot u_i^*}{\Delta t} = \frac{\text{Vol} \cdot u_i^n}{\Delta t} - C_i^{n+1/2} + D_i^{n+1/2} - G_i(p^{n+1/2}) \quad (15)$$

where Vol is the volume of the cell, Δt is the time step between time step n and $n+1$. C_i and D_i are the volume integrated convection and diffusion term, respectively. $G_i(\phi)$ is a discretised operator which computes volume integrated gradient of the scalar ϕ in the x^i direction (in the equation ϕ is equal to p). All the spatial operators are given in the Appendix.

The integrated convective term C_i is found by QUICK interpolation. In the original fractional step methods the

explicit Adams–Bashforth method is used for predicting $C_i^{n+1/2}$. This is also the case in this application:

$$C_i^{n+1/2} = \frac{1}{2} \left(3 \sum U^{j,n} \cdot Q(u_i^n) - \sum U^{j,n-1} \cdot Q(u_i^{n-1}) \right) \quad (16)$$

where $U^{j,n}$ is the flux into the cell domain at face j at time step n and Q^j denotes the QUICK interpolation operator over the cell faces, i.e. $Q^j(u_i^n)$ gives the QUICK interpolated value of u_i at cell face j which is convected into the cell by the cell face flux $U^{j,n}$, see above.

For the diffusive term D_i in Eq. (15) a mixed central and Adams–Bashforth method is used:

$$D_i^{\text{impl}} = \frac{1}{2} \sum_j S1_i^j(u_i^*)$$

$$D_i^{\text{expl}} = \frac{1}{2} \sum_j S1_i^j(u_i^n) + \frac{1}{2} \left(3 \sum_j S2_m^j(u_i^n) - \sum_j S2_i^j(u_m^{n-1}) \right) \quad (17)$$

where ν is the kinematic viscosity and S1 and S2 are special terms of the viscous stress tensor found from the stress tensor defined as:

$$S_i^j = \nu \left(\frac{\partial u_i}{\partial x_k} + \frac{\partial u_k}{\partial x_i} \right) n_k^j. \quad (18)$$

The diffusion term is then found as integration over the cell faces. An implicit treatment of Eq. (18) would result in a very

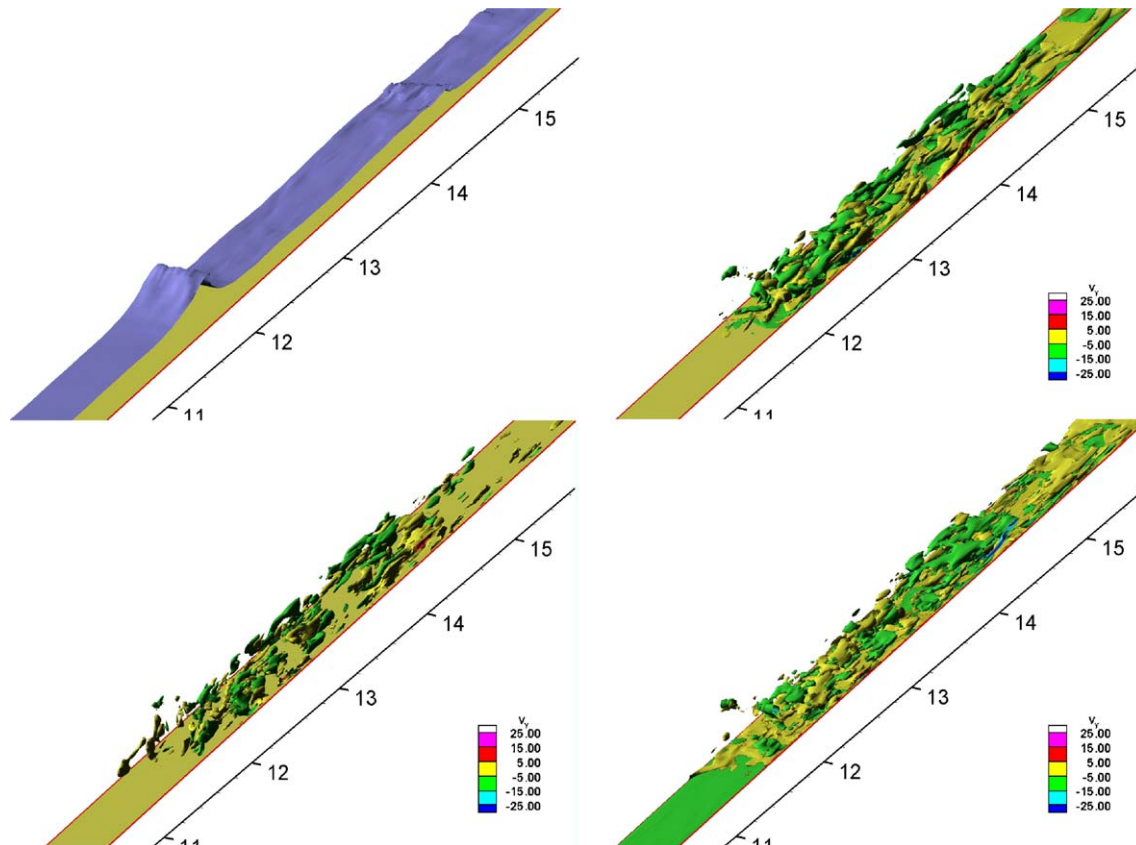


Fig. 3. An example of the free surface and vorticity for the spilling breaker after 19 wave periods after the start of the simulation. The x -axis is along the flume, the y -axis is the vertical direction, and the z -axis is the transverse direction.

The found velocities and fluxes have to be modified at the surface according to the free surface method described in the next section.

Now the velocity field and the position of the free surface are known at time step $n+1$. In a traditional fractional step method the pressure could be updated by the pressure correction term ϕ . In usual fractional step methods, the pressure forcing is evaluated in the predictor step and is updated in time by the incrementation procedure.

Step 5:

The absolute value of the pressure field has to comply accurately with the dynamic free-surface condition. This is not possible since the pressure at time step n was found for another position of the surface. Instead another pressure equation is set-up. It is known that the velocity at time step $n+1$ and time step n fulfills the continuity equation, therefore the divergence of the convective and diffusive terms has to be equal to the pressure gradients. That gives the following Poisson equation for the pressure that is solved in the same manner as the one for the pressure correction term.

$$U_{\text{mom}}^{j,n+1} = I_F(-C_i^{n+1} + D_i^{n+1}) \cdot n_i^j, \quad (22)$$

$$\sum_j G^j(p^{n+1}) = \sum_j U_{\text{mom}}^{j,n+1}.$$

All computations are carried out with a variable time increment, Δt , at every time step keeping the maximum cell Courant number within the limit $U\Delta t/\Delta x < C_{\text{cf}}$, the courant number being $C_{\text{cf}}=0.25$. Smaller time steps have not shown to give different results of for instance the breaking point and the averaged quantities such as the undertow profiles. Basically, using a time step smaller than the specified Courant number is rather restrictive for the major part of the flow as it is the minimum of all the cells that determines the time step.

2.2.2. Solution of algebraic equations

The implicit part of the discretised momentum Eq. (15) is written with 7-point stencils, whereas the Poisson Eqs. (20) and (22) are written with 19-point stencils in a cell-by-cell form. Line relaxation techniques solve the discretised momentum equation, while the Poisson Eqs. (20) and (22) are solved by a multigrid method or a Preconditioned Conjugate Gradient method with a multigrid smoother as the pre-conditioner. The

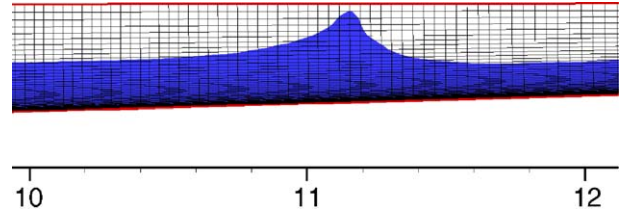


Fig. 7. Close view of the coarse grid resolution around the breaking point.

multigrid smoother uses a standard coarsening and V-cycle relaxation. On every multigrid level an ILLU smoother is employed. A general introduction to these techniques can be found in Ferziger and Peric (1999).

2.3. Volume of fluid (VOF)

Since the Navier–Stokes equations are solved on a rigid grid, the free surface has to cut through the cells. An approach that has become very popular during recent years is based on a continuity equation for a conservative quantity, F , as sketched by the following equation:

$$\frac{\partial F}{\partial t} + \frac{\partial u_i F}{\partial x_i} = 0. \quad (23)$$

The fluid is located where F is equal to 1.0 and the air/void region where it is equal to 0. $F=0.5$ determines the position of the free surface.

Eq. (23) is solved in a Eulerian way. A straightforward way to solve the problem is to use a very accurate higher order convection scheme such as the QUICK or even higher. Kawamura and Miyata (1994) used this approach. In their case both the air and fluid flow were simulated around ships and submerged bodies. In Hirt and Nichols (1981), a special advection scheme was used for avoiding the smearing of the surface, which they called the “Volume of Fluid” also known as VOF. This method has been extensively used and modified by several researchers.

The scheme introduced by Hirt and Nichols (1981) was later modified and improved by Ubbink (1997). The Compressive Interface Capturing Scheme for Arbitrary Meshes, CICSAM, was developed by Ubbink (1997) and is a blending of Hyper-C, Leonard (1991), the upper bound of the convection boundedness criteria (CBC), and ULTIMATE-QUICKEST Leonard (1991), the transient bounded version of QUICK. The blending

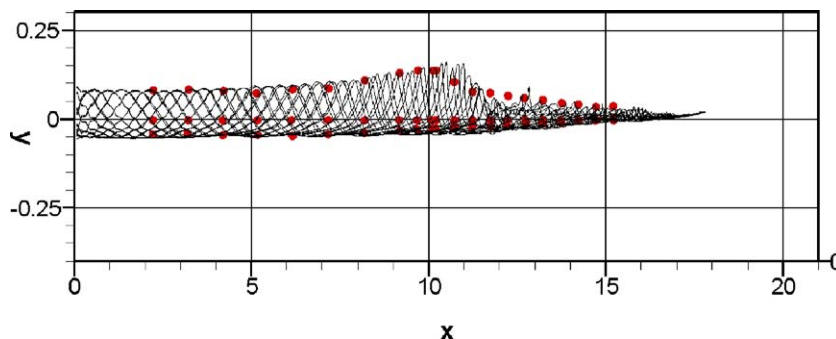


Fig. 6. Envelope of water surface from 28 to 32 s. Spilling breaker with the k -equation sgs formulation. Dimensions in m.

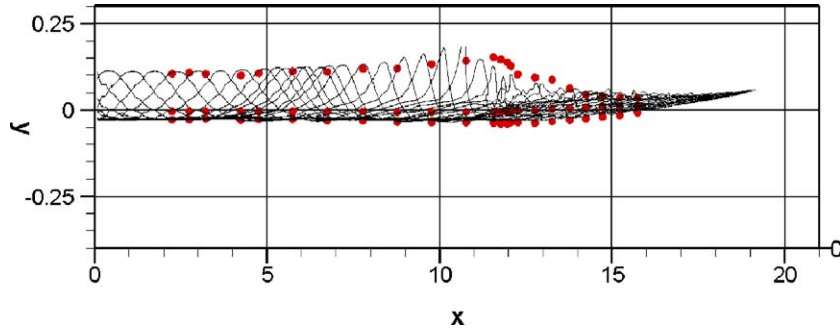


Fig. 8. Envelope of a plunging breaker, Smagorinsky sgs model. Dimensions in m.

of the schemes is determined by the orientation of the interface and the flow direction. The full description of the method is rather comprehensive and the reader is advised to consult the original PhD-thesis for a more detailed description of the method.

2.3.1. Time integration

The time integration of the function F follows the second order Adams–Bashforth scheme, which was the same scheme used for the momentum equations. Eq. (24) shows the scheme with the use of the VOF scheme for the spatial fluxing of the quantity F .

$$F^{n+1} = F^n - \Delta t \frac{1}{2} \left(3 \sum_j F_{\text{flux}}^{j,n} - \sum_j F_{\text{flux}}^{j,n-1} \right). \quad (24)$$

When the CICSAM advection scheme is applied the Adams–Bashforth scheme is applied on the fluxes instead (i.e. the velocity fluxes as determined in Eq. (16)). This is due to a predictor-corrector step in the CICSAM that would be violated if the Adams–Bashforth scheme was applied on the F fluxes. In the estimation of F^{n+1} it is the predicted fluxes at $n+1/2$, that are used, wherefore the prediction of F becomes nearly of 2nd order.

2.3.2. Boundary conditions for the pressure at the free surface

The fulfillment of Eq. (23) is a way to satisfy the kinematic boundary condition. The surface tension has been neglected, whereby setting the pressure equal to the atmospheric pressure or as an approximation equal to 0 satisfies the dynamical boundary condition at the free surface.

Instead of specifying the exact pressure at the surface a Dirichlet boundary condition for the excess pressure is applied as:

$$p_{\text{surface}} = p_{\text{atm}} - \mathbf{g} \cdot (\mathbf{r}_{\text{surface}} - \mathbf{r}_0) \quad (25)$$

where \mathbf{g} and p_{atm} denote the gravitational force vector and the atmospheric pressure in the air (normalised by fluid density), respectively. $\mathbf{r}_{\text{surface}}$ is the vector from origo to the surface, and \mathbf{r}_0 a vector from origo to the still water level. In the present work the atmospheric pressure is set to zero, $p_{\text{atm}} = 0$. In this way the inclusion of a gravitational term in the Navier Stokes equations is avoided.

3. Computational set-up

The computational domain consists of a 3 m flat bed followed by a slope of 1:35. The water depth before the slope is 0.4 m. The computational domain reflects the physical tests presented in Ting and Kirby (1994), with a minor difference. In their experiments the slope was started with a small step of 0.02 m, however, this difference is assumed not to have any significant influence on the comparison between measurements and numerical results.

Fig. 1 shows the computational domain. The width of the domain is 0.3 m. The curvilinear grid consists of $320 \times 48 \times 32$ cells (longitudinal, nearly vertical, transverse). It is stretched towards the bed and towards the area of initial breaking. The relatively coarse grid is shown in Fig. 2. The choice of a finer grid resolution is limited by the number of different scenarios that should be simulated and the length of

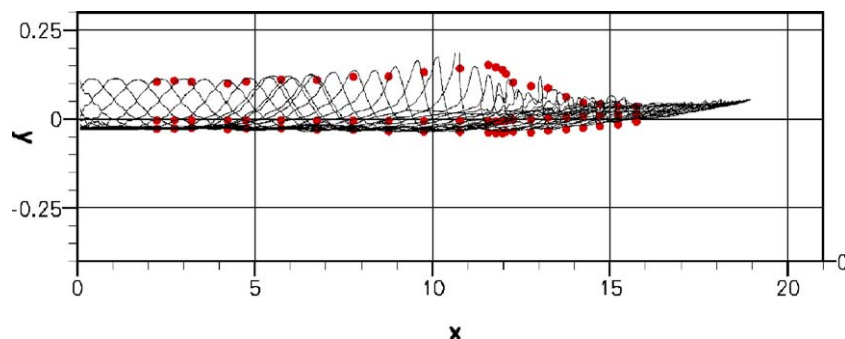


Fig. 9. Envelope of a plunging breaker, k -equation sgs model. Dimensions in m.

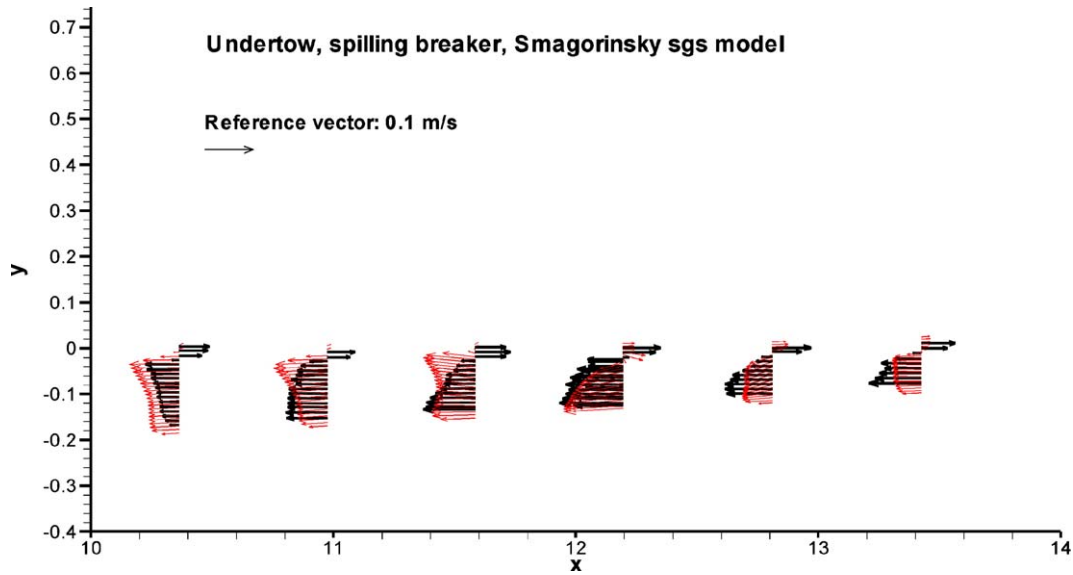


Fig. 10. Undertow profile under a spilling breaker compared to the measurements of Ting and Kirby (1994). The Smagorinsky sub-grid scale model was used.

the simulations. The main purpose of this study is to model realistic scenarios of breaking waves in the surf zone with a full three-dimensional model based on Large Eddy Simulation. The computations have been carried out on fast PCs, however, the possibility of using supercomputers such as a parallel computer would enhance the capability of performing this kind of computations.

4. Results

The table below gives the wave parameters for the different scenarios that are investigated, which are spilling and plunging breakers (Table 1).

The waves are based on fifth order Stokes and Cnoidal wave theory. For the spilling breaker fifth order Stokes theory is valid, while Cnoidal theory is valid for the plunging breaker at the inlet boundary. Both the velocities and the surface elevation are specified at the ‘inlet’ boundary.

4.1. Flow structures and envelope

To give an indication of the results the free surface and the vorticity around the three axes are shown in Fig. 3. In the inner part of the surf zone high levels of vorticity are present. The *x* and *z* components of the vorticity are relatively strong, which could be linked to longitudinal and transverse eddies. It

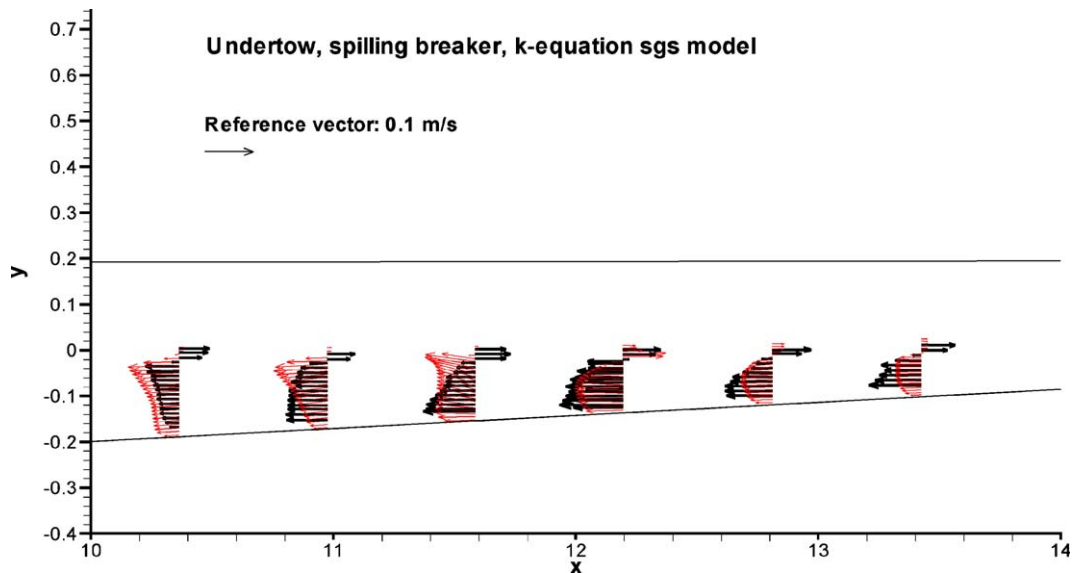


Fig. 11. Undertow profile under a spilling breaker compared to the measurements of Ting and Kirby (1994). The *k*-equation sub-grid scale model was used.

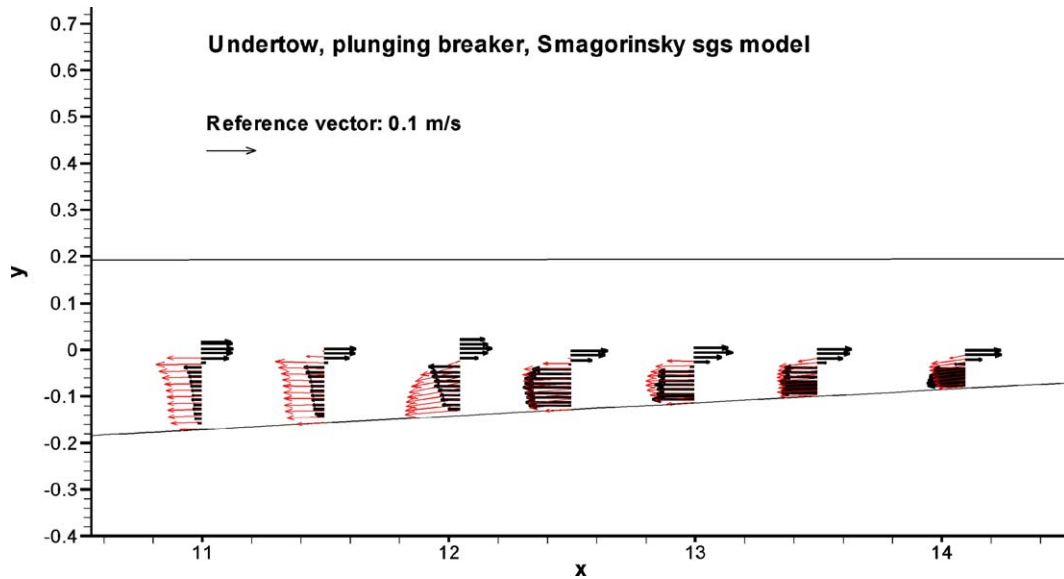


Fig. 12. Undertow profile under a plunging breaker compared to the measurements of Ting and Kirby (1994). The Smagorinsky sub-grid scale model was used.

could be argued that the x -component to some extent represents obliquely descending eddies as observed in for instance Nadaoka et al. (1989).

Fig. 4 shows the vorticity around the three axes under the plunging breaker. Compared to the spilling breaker the vorticity almost disappears between the two breakers. Especially the vorticity around the vertical axis is non-existent around $x = 15$ m. Just under the broken waves all three vorticity components are rather strong. As the major part of the turbulent kinetic energy is related to eddies the results indicate that the turbulence is relatively evenly distributed under the spilling breaker and located under the breaker in the plunging breaker case. This is in good agreement with turbulent kinetic energy

measurements in Ting and Kirby (1994). The study of the vortex dynamics has been limited to these few qualitative observations. A more detailed qualitative study is not given here as the focus is on the undertow and turbulence.

Figs. 5 and 6 show the envelope of the wave for the spilling breaker for the Smagorinsky and k -equation sgs models, respectively. The agreement is quite good except just after the laboratory breaking point. Here the wave heights are over-predicted for both sgs turbulence models. The initiation of breaking is too late which explains the larger wave heights just after the laboratory flume breaking point. The coarse resolution of the fluid domain is the main reason for that, cf. Fig. 7. The wave top is only resolved by a few computational cells.

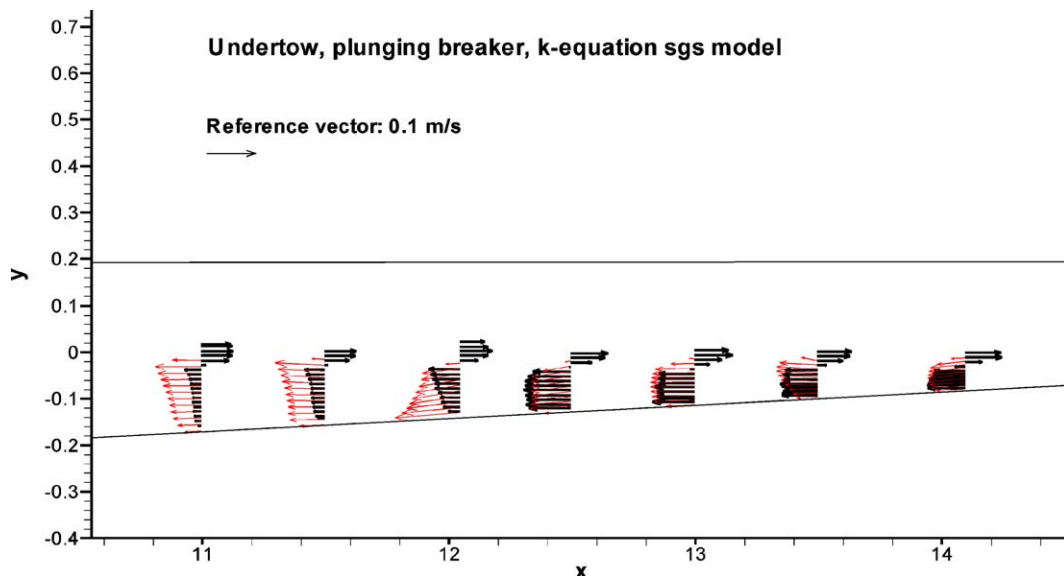


Fig. 13. Undertow profile under a plunging breaker compared to the measurements of Ting and Kirby (1994). The k -equation sub-grid scale model was used.

Therefore the breaking is delayed in the spilling breaker case. However, the resolution has been a choice between acceptable computational turn around times, sufficient resolution close to the bed to resolve the effect of the wave boundary layer, and sufficient resolution of the initial breaker. The present work focuses on the generation of undertow and turbulence quantities under the broken wave and therefore a rather coarse resolution was necessary in the upper part of the wave. As the waves break too late in the spilling breaker case the analyses of undertow and turbulence will focus on the inner part of the surf zone. The breaking point is rather sensitive to for instance imperfections in the wave generation and the effect of the previous broken wave. It could be argued that this gives an artificial contribution to the turbulence, as discussed in Nadaoka et al. (1989).

The picture for the plunging breaker is slightly different from the spilling breaker as the waves break too early in this

case, of Figs. 8 and 9. This results in a large wave height before the laboratory breaking point and too early breaking. No major difference is seen between the two different sgs turbulence models. In the inner part of the surf zone a reasonable agreement is found between the measured and modelled wave envelopes. Again this suggests that the analysis should focus on the inner part of the surf zone.

4.2. Undertow

During the breaking process potential wave energy is transformed into kinetic energy where a part of the water in the top of the wave is thrown in front of the wave or rushes down from the wave top. The water is transported towards the shoreline in the upper part of the water column. This results in a set-up that generates an offshore directed flow under the still water level called the undertow, and hereby continuity of mass

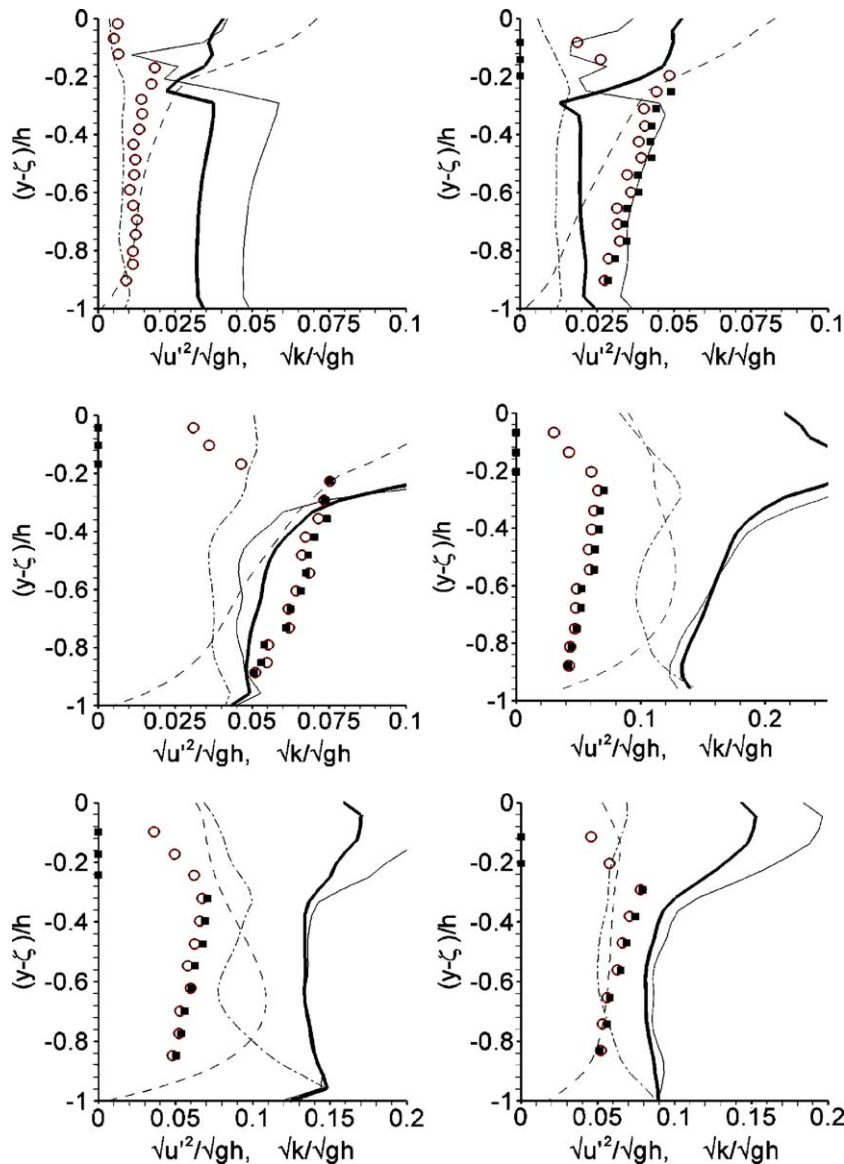


Fig. 14. Comparison of average turbulence levels for the spilling breaker with the Smagorinsky sgs model. \blacksquare : Modelled $(k/gh)^{1/2}$, \blacksquare measured $(k/gh)^{1/2}$, — : modelled $(\overline{u^2}/gh)^{1/2}$, \circ : measured $(\overline{u^2}/gh)^{1/2}$, -- -- : modelled $(\overline{v^2}/gh)^{1/2}$, - - - : modelled $(\overline{w^2}/gh)^{1/2}$.

will be fulfilled. The undertow is found by averaging the flow velocities over the transverse direction for the last 5 wave periods of the simulations.

Figs. 10 and 11 show the undertow profiles under the spilling breaker based on the Smagorinsky sub-grid scale model and the k -equation sub-grid scale model, respectively. The simulated undertow profiles are of the same order of magnitude as the measured undertow profiles. The shift between the onshore directed and the offshore directed flow over the vertical is located at the same place as in the experiments. This shows that the overall continuity equation is fulfilled.

The shape or gradient of the velocity profiles is determined by the mixing of momentum. If the mixing is large the gradient ($\partial u / \partial z$) will be close to zero and increase as the mixing decreases. The mixing in standard RANS models like for instance the $k-\omega$ model is maintained through the eddy viscosity. In LES a major part of the mixing of momentum

takes place through the large-scale eddies and the eddy viscosity accounts for a minor part. It is quite clear from the figures that the vertical gradient ($\partial u / \partial z$) in the simulated velocity profiles is smaller than the one found from measurements in the inner part of the breaking zone. This might be due to a stronger mixing in the simulations compared to the measurements.

In the inner part of the breaking zone good agreement is found at around $x=12$ m. Here the undertow profile has almost the same gradient in the experiment as found in the simulations. The differences between the results obtained with the two different sgs models are very small. Further inshore at $x=13.4$ m the profiles are slightly different, where the gradient of the modelled undertow is smaller than the one found in the experiment.

The undertow profiles for the plunging breaker are shown in Figs. 12 and 13. In the inner part of the breaking zone a very good agreement between the model and the experiments is found. The Smagorinsky sgs model performs slightly better

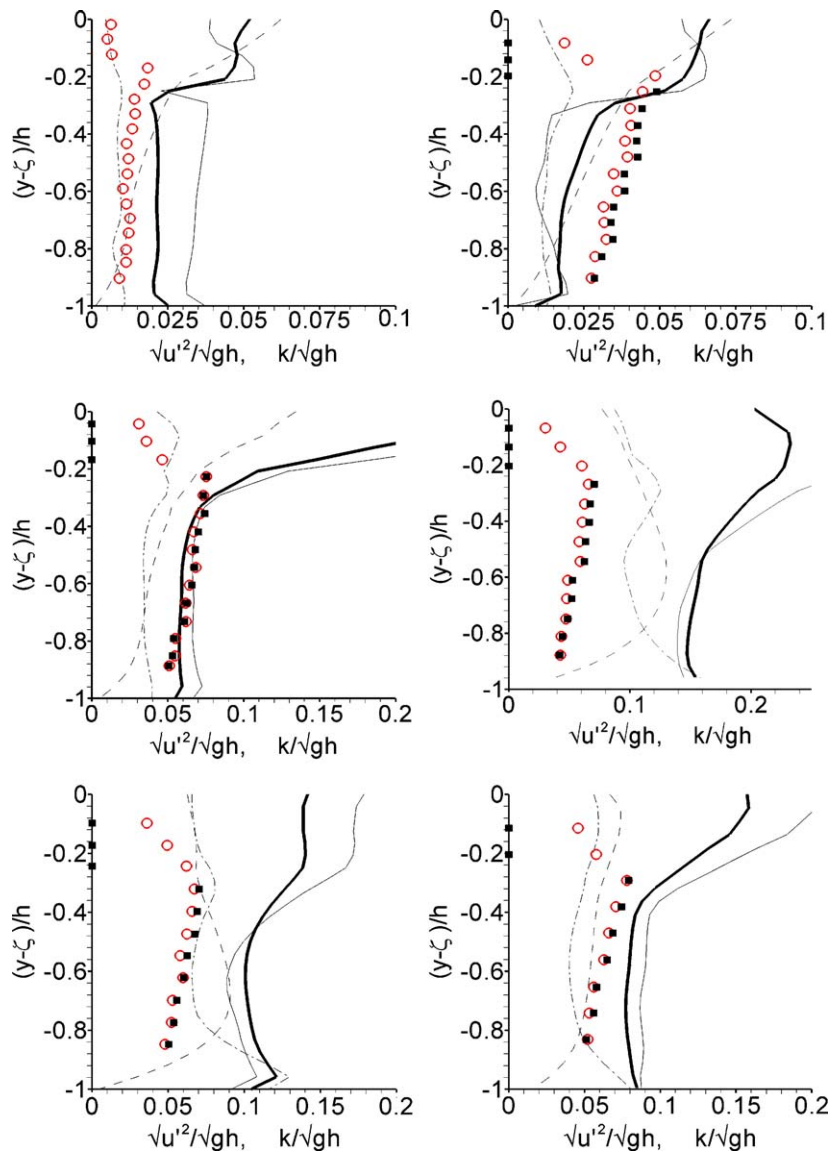


Fig. 15. Comparison of average turbulence levels for the spilling breaker with the k -equation sgs model. \blacksquare : Modelled $(k/gh)^{1/2}$, \blacksquare : measured $(k/gh)^{1/2}$, — : modelled $(\overline{u^2}/gh)^{1/2}$, \circ : measured $(\overline{u^2}/gh)^{1/2}$, --- : modelled $(\overline{v^2}/gh)^{1/2}$, --- : modelled $(\overline{w^2}/gh)^{1/2}$.

than the k -equation sgs model at $x=13.5$ m. In the outer part of the breaking zone the simulations over-predict the strength of the undertow compared to the measurements. Earlier it was found that the wave in this case breaks too early. Therefore water is transported towards the shoreline in the upper part of the water column and it has to be compensated with a stronger undertow.

4.3. Turbulence levels

For each phase the components are averaged in the transverse direction. The average of the quantity can therefore be interpreted as belonging to the ordered motion and the deviation from the average as the turbulent fluctuation. This analysis has the advantage that a detailed spatial distribution of the turbulence can be obtained from few data sets with the instantaneous velocities from the entire computational

area. Furthermore, the data are phase averaged for the last five wave periods in order to improve the statistics. The use of the transverse direction in estimation of the turbulence was discussed in detail in Christensen and Deigaard (2001). If the dimension in the transverse directions is infinitely long the estimation of turbulence could be determined as the deviation from the average taken in that direction. Therefore using the transverse direction together with ensemble averaging reduces the necessary number of periods to achieve stable statistics. Whether 5 wave periods are sufficient is a question that is difficult to answer as only 20 and 16 wave periods are simulated. However, a few tests with 7 periods gave turbulence levels within the same range. Therefore the averaging technique is found adequate in the comparison to the measurements by Ting and Kirby (1994). The study by Christensen et al. (2000) indicated that stable statistics in the numerical model were obtained after around

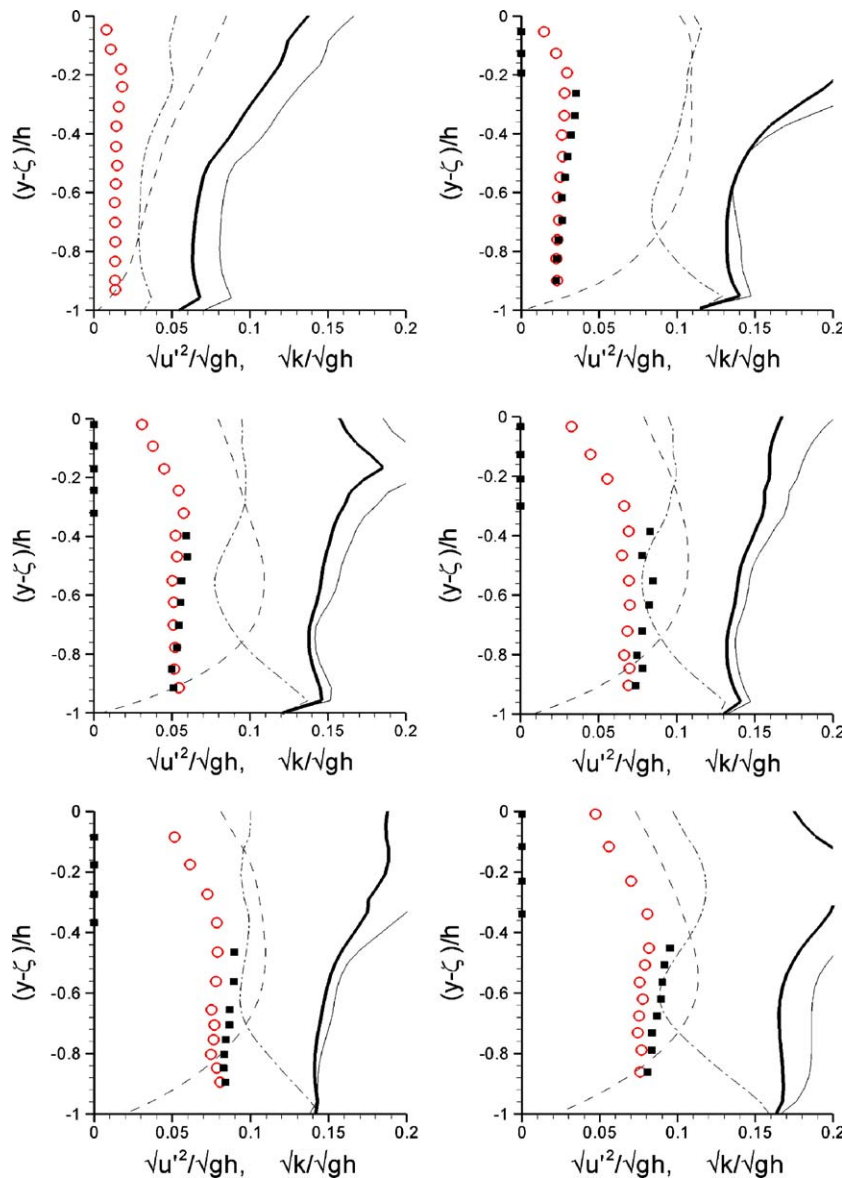


Fig. 16. Comparison of average turbulence levels for the plunging breaker with the Smagorinsky sgs model. ■: Modelled $(k/gh)^{1/2}$, ■ measured $(k/gh)^{1/2}$, —: modelled $(u^2/gh)^{1/2}$, ○: measured $(u^2/gh)^{1/2}$, - - -: modelled $(v^2/gh)^{1/2}$, - - -: modelled $(w^2/gh)^{1/2}$.

15 wave periods after start of the simulation. Note that it was with a two-dimensional RANS two-equation turbulence model and therefore the conclusion might not be applicable in this case.

The velocity is thus split into a mean quantity, \bar{u} , averaged in the direction parallel to the coastline and phase averaged over the last five wave periods in the simulations, and a turbulent fluctuation, u' :

$$u = \bar{u} + u' \tag{26}$$

and the turbulent fluctuation on the grid scale is:

$$k_{GS} = 1/2(\overline{u'^2} + \overline{v'^2} + \overline{w'^2}) \tag{27}$$

However, this only accounts for the turbulence resolved by the computational grid. The full turbulence level is found by adding the sub-grid scale turbulence. For the k -equation this is straightforward as the k_{sgs} is calculated as a part of the

computations. For the Smagorinsky model the sub-grid scale turbulence is estimated from the sgs viscosity and the corresponding mixing length as the length scale:

$$k_{sgs} = \left(\frac{\nu_{sgs}}{C_s \Delta} \right)^2 \tag{28}$$

The total amount of turbulence is:

$$k = k_{GS} + k_{sgs} \tag{29}$$

After the phase averaged turbulence levels the quantities were averaged over the entire wave period for comparison with the measurements in Ting and Kirby (1994). It is the turbulence kinetic energy given by Eq. (29) that is compared to the measurements in Ting and Kirby (1994). It should be noted that in Ting and Kirby (1994) the total turbulent kinetic energy is set equal to $k = \frac{1}{2}(\overline{u'^2} + \overline{v'^2}) + \frac{1}{3} \frac{1}{2}(\overline{u'^2} + \overline{v'^2})$,

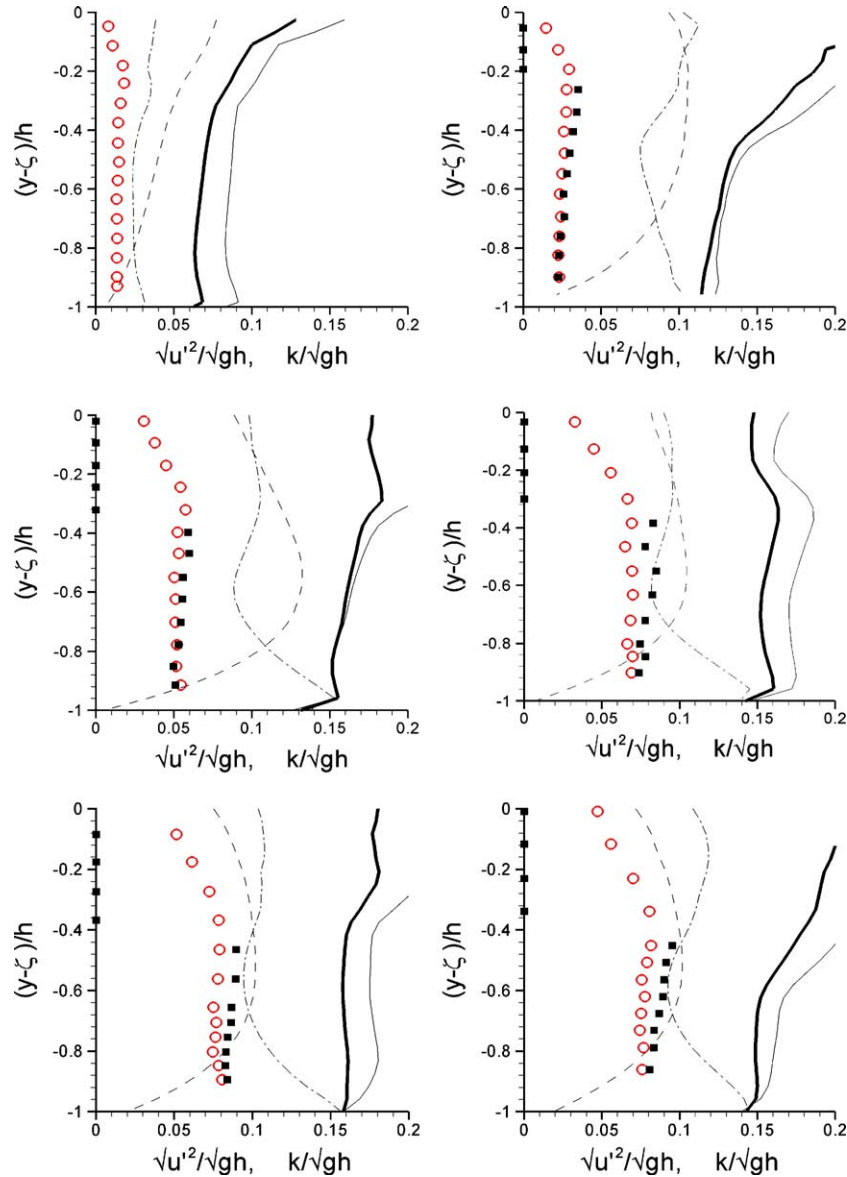


Fig. 17. Comparison of average turbulence levels for the plunging breaker with the k -equation sgs model. \blacksquare : Modelled $(k/gh)^{1/2}$, \blacksquare measured $(k/gh)^{1/2}$; \bullet : modelled $(\overline{u'^2}/gh)^{1/2}$, \circ : measured $(\overline{u'^2}/gh)^{1/2}$, $---$: modelled $(\overline{v'^2}/gh)^{1/2}$, $---$: modelled $(\overline{w'^2}/gh)^{1/2}$.

where it is assumed that $\overline{w'^2} = \frac{1}{3} \frac{1}{2} (\overline{u'^2} + \overline{v'^2})$. This assumption has been used in several studies as Stive (1980), Svendsen (1987), and Ting and Kirby (1994, 1995, 1996) among others. The assumption will be discussed later in this chapter.

Figs. 14 and 15 show the comparison between the measured and simulated averaged turbulence levels for the Smagorinsky and k -equation sub-grid scale model, respectively. Note that the velocity component along the flume is u , the vertical v , and the transverse w . The panels show the turbulence levels at $x=10.365, 10.975, 11.585, 12.195, 12.81, 13.425$ m. The first panel is outside the actual breaking zone. Here the simulated levels are larger than the measured one. Especially the u -component tends to be large. This could be due to turbulent flow configurations that have not been dissipated before it is convected offshore from the breaking

zone. The k -equation seems to give smaller turbulence levels at this position. In the Smagorinsky model the dissipation of energy through the sub-grid scale eddy viscosity is directly linked to the local strain rate whereas the eddy viscosity in the k -equation sgs model can be effected by previously produced turbulence energy. Therefore it continues to dissipate energy even in regions where the strain rate locally is small. This leads to an increased dissipation of turbulent kinetic energy outside the breaking zone and therefore a better prediction of the turbulence levels in these regions. In the inner part of the breaking zone the average turbulence levels are in the order of two times larger than the measured ones.

Figs. 16 and 17 show similar results for a plunging breaker found with the Smagorinsky and k -equation sub-grid scale model, respectively. The panels show the turbulence levels at

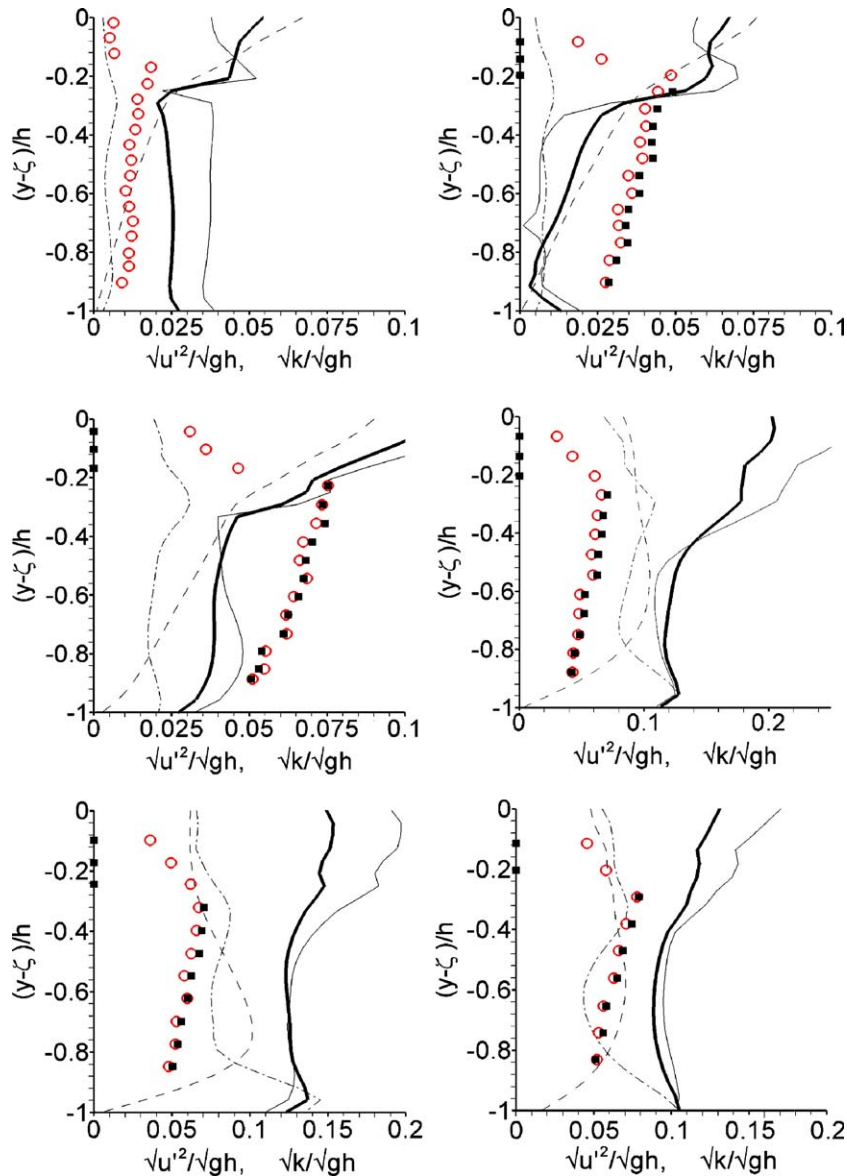


Fig. 18. Comparison of average turbulence levels for the spilling breaker with the Smagorinsky sgs model. In this case the Smagorinsky constant C_s was equal to 0.2. \blacksquare : Modelled $(k/gh)^{1/2}$, \blacksquare measured $(k/gh)^{1/2}$, — : modelled $(\overline{u'^2}/gh)^{1/2}$, \circ : measured $(\overline{u'^2}/gh)^{1/2}$, --- : modelled $(\overline{v'^2}/gh)^{1/2}$, --- : modelled $(\overline{w'^2}/gh)^{1/2}$.

$x=10.995, 11.495, 12.045, 12.995, 13.495, 14.095$ m. The first panel is outside the actual breaking zone. In this case the simulated turbulence levels are at all panels larger than found in the measurements. As shown earlier the plunging breaker starts to break too early compared to the measurements. Therefore the production of turbulent kinetic energy starts earlier as well. In the inner surf zone the turbulence levels are found to be around twice as large as the levels found in the experiments.

The high levels of turbulent kinetic energy seem to be one of the main problems in simulating breaking waves. Therefore an additional test case was made for the spilling breaker with a Smagorinsky constant equal to $C_s=0.2$. However, this did not change the result significantly, cf Fig. 18.

For the plunging breaker case another way of estimating the turbulence was tested. In that case the turbulence was only related to the deviation from the mean velocity taken in the

transverse direction. This means that the phase averaging is omitted. The turbulence levels were averaged over the last 5 wave periods of the simulation. It was pointed out by Nadaoka et al. (1989) that the turbulence in the surf zone from one breaking wave to another may affect the exact position of the breaking point of the next, thereby adding a non-deterministic component. Fig. 19 compared to Fig. 16 shows that the difference between the turbulence between the phase averaged values and the ones without phase averaged values is very small. Therefore the major contribution to the turbulence stems from turbulent fluctuations that have a much smaller time-scale than the wave period. Furthermore, the non-deterministic but ordered velocity contribution that was discussed in Nadaoka et al. (1989) has only little influence on the levels of turbulence. Therefore the approach by using phase averaged quantities in order to find the turbulence levels in periodic breaking waves is a sufficient approach.

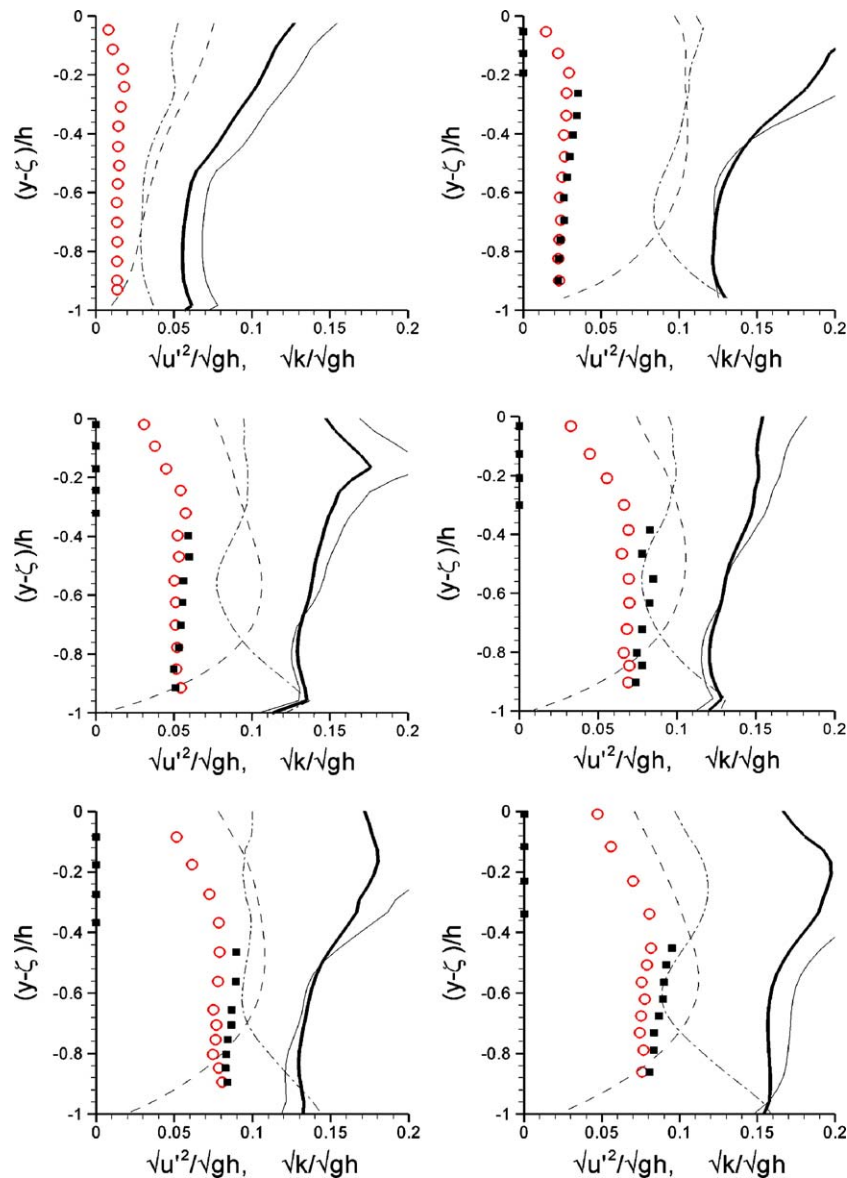


Fig. 19. Comparison of average turbulence levels for the plunging breaker with the Smagorinsky sgs model. **—**: Modelled $(k/gh)^{1/2}$, **■** measured $(k/gh)^{1/2}$, **—**: modelled $(\overline{u^2}/gh)^{1/2}$, **○**: measured $(\overline{u^2}/gh)^{1/2}$, **- - -**: modelled $(\overline{v^2}/gh)^{1/2}$, **- · -**: modelled $(\overline{w^2}/gh)^{1/2}$.

In Ting and Kirby (1994) only the horizontal and the vertical velocity components were measured. Therefore they used the following relation to estimate the turbulence levels:

$$k = 1.33/2 \cdot (\overline{u'^2} + \overline{v'^2}) \tag{30}$$

This relationship was also used by Stive and Wind (1982) and discussed in Svendsen (1987) and found adequate based on similarity between a spilling breaker and a plane wake.

It is straightforward to test this assumption in this case and two examples are shown in Fig. 20.

In the spilling breaker case the assumption is in good agreement with the direct estimation of turbulence intensity. However, close to the bed at the breaking point the assumption gives a rather low prediction of the turbulence level. This might be explained by the generation of large-scale turbulent flow

structures at this point, which cannot be represented by the simple approximation.

In the plunging breaker case Eq. (30) over-predicts the turbulence level in the middle of the water column whereas closer to the bed a good agreement is achieved. The reason for disagreement is due to a different distribution of the turbulence on the components $\overline{u'^2}$, $\overline{v'^2}$, and $\overline{w'^2}$. When examining Figs. 14–17 it appears that the square root of the turbulent component $\sqrt{\overline{u'^2}}$ is in the order of 1.5 times larger than the other two components $\sqrt{\overline{v'^2}}$ and $\sqrt{\overline{w'^2}}$ whereas the factor is in the order of 1.75 in the plunging breaker case.

In Eq. (30) a factor of 1.5 seems reasonable since the square is approximately 2 and therefore the transverse component can be set equal to $\frac{1}{3} (2 \cdot \overline{w'^2} + \overline{v'^2}) \cong \frac{1}{3} (2 \cdot \overline{u'^2} + \overline{v'^2})$.

In the plunging breaker case the following relationship seems more correct from the analysis: $\frac{1}{4} (3 \cdot \overline{w'^2} + \overline{v'^2}) \cong \frac{1}{4} (2 \cdot \overline{u'^2} + \overline{v'^2})$ which shows a clear difference in the turbulent structure between spilling and plunging breakers.

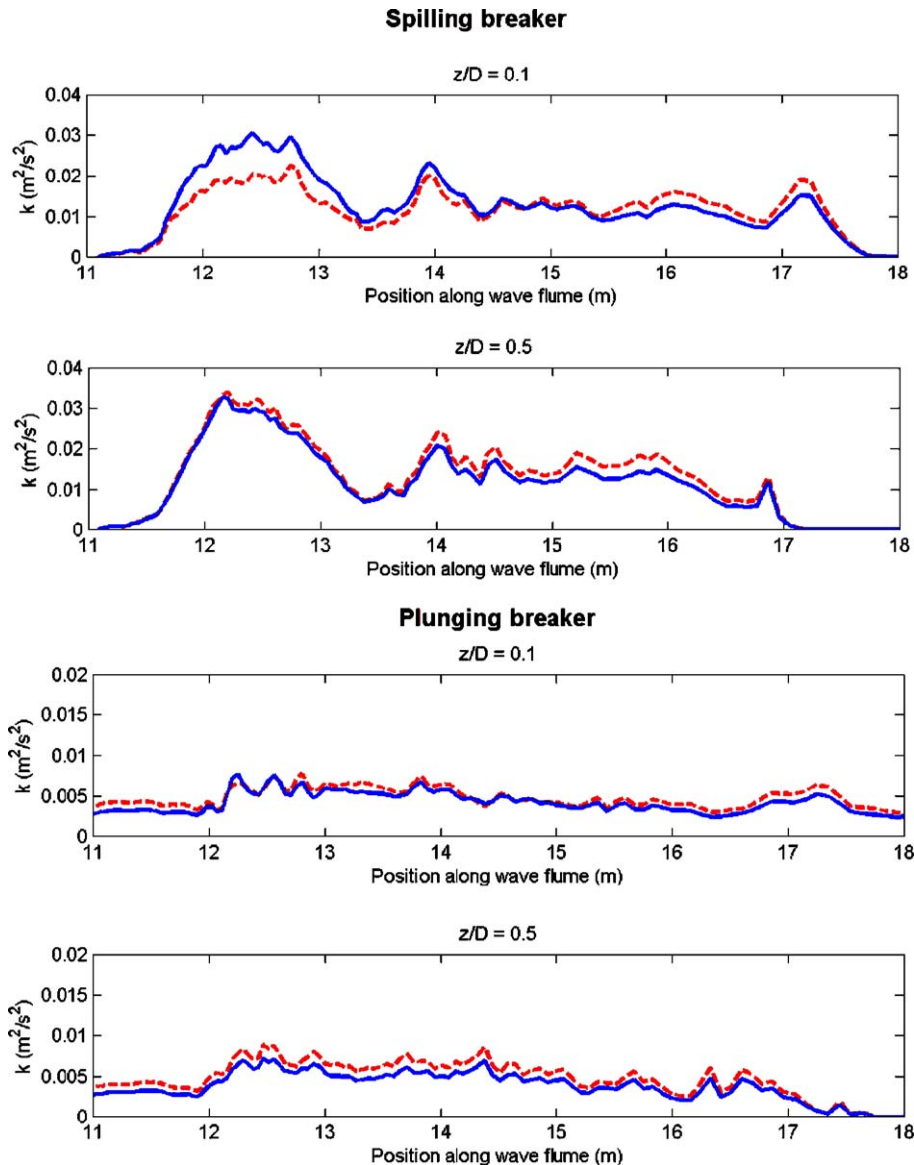


Fig. 20. Comparison of the modelled (—) average turbulence intensity to the relation given in Eq. (30) (---).

5. Concluding remarks

The set-up, undertow, and turbulence levels have been studied with a Navier–Stokes solver with a free surface. The turbulence simulation is based on the Large Eddy Simulation concept where the major part of the turbulence kinetic energy is simulated while the small-scale energy is modelled by a sub-grid scale model. The computations are full three-dimensional and therefore very time-consuming since a number of wave periods have to be modelled in order to achieve stable statistics.

There is a good agreement between the modelled and measured set-up in the inner part of the surf zone. However, the exact breaking point is not captured in the simulations due to the coarse resolution, and therefore some discrepancies are seen close to the breaking point. The modelled undertow profiles have a smaller gradient (du/dy) than found in the experiments. This may be explained by a stronger mixing in the simulations than in the experiments.

The reason for the stronger mixing is difficult to point out. The coarse resolution might be a part of the explanation. However, the effect of air has not been modelled at all. The mixture of air and water in the upper part of the water column perhaps dissipates a major part of the energy before it penetrates down through the water column.

As it is found that the mixing is too strong it is not surprising that the turbulence levels in general were too high compared to the measurements. It is found that the simplification in estimating the turbulent kinetic energy in spilling breaking from two velocity components is sufficient in the inner part of the surf zone, whereas the assumption might not be valid in plunging breakers.

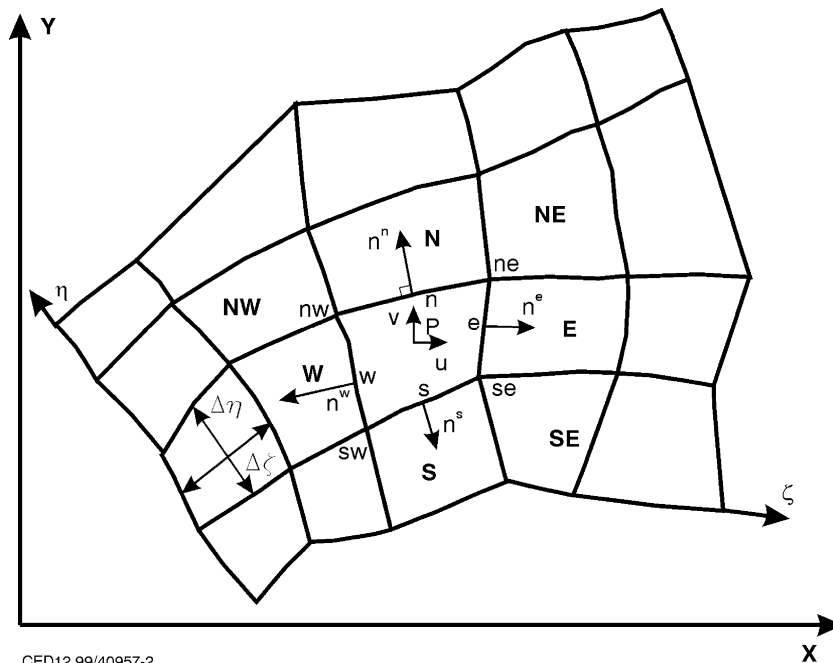
Acknowledgements

The author would like to acknowledge the support, partly funded by the Danish Technical Research Council (STVF grant no. 9801635) under the frame programme Computational Hydrodynamics. The work was also partly funded by the Commission of the European Communities Directorate General for Science Research and Development on the Environmental Design of Low Crested Coastal Defence Structures (DELOS) project under contract number EVK3-CT-2000-00041. The Navier–Stokes solver was originally developed at ICCH (International Research Centre for Computational Hydrodynamics, located at DHI from 1994 to 1998), by Stefan Mayer, Takafumi Kawamura, Lars S. Sørensen, and Antoine Garapon. They are acknowledged for their great effort.

Appendix A. Spatial discretisation

Due to the complexity of showing all three dimensions in a plane plot some of the explanations will be based on illustrations in two dimensions. However, the extension to three dimensions is rather straightforward.

The discretisation uses two co-ordinate systems; one related to the physical orientation (x, y, z) and another that follows the mesh lines (ξ, η, ζ), as sketched in Fig. A.1. In three dimensions the sup-scripts refer to the cell numbering in the structured grid (i, j, k) and the sub-scripts to the global co-ordinate system (x, y, z). For instance the velocities u, v, w and the pressure are located at cell centres and the velocities relate to the physical co-ordinate system (x, y, z). The fluxes through the cell faces U_i are related to the (ξ, η, ζ) co-ordinate system.



CED12.99/40957-2

Fig. A.1. Sketch of the structured non-orthogonal grid situated in a global co-ordinate system. Sup-scripts refer to the structured grid (ξ, η) and sub-scripts to the component in the x or y direction in the global co-ordinate system (x, y) in two dimensions.

The discretisation is described by a number of operators. For simplicity the discretisation is given in two dimensions in the following.

A.1. Interpolation operators

Linear interpolation (or central interpolator) where I_F denotes the averaging operation which interpolates a value of cell centred variables to cell faces. n_i^j is the i -component ((x, y) co-ordinate system), e denotes the east cell face.

$$I^e(\phi) = \frac{1}{2}(\phi_{i,j} + \phi_{i+1,j}) \tag{A.1}$$

The QUICK interpolation operator, which is a third order upwind scheme of the spatial discretisation, looks as:

$$\begin{aligned} Q^w(u_i) &= \frac{1}{2}(u_{i,j} + u_{i-1,j}) - \frac{1}{8}(u_{i-2,j} - 2u_{i-1,j} + u_{i,j}) \\ Q^e(u_i) &= \frac{1}{2}(u_{i+1,j} + u_{i,j}) - \frac{1}{8}(u_{i-1,j} - 2u_{i,j} + u_{i+1,j}) \end{aligned} \tag{A.2}$$

where w and e refer to the western and eastern cell face, respectively. An example is given in Fig. A.2.

The use of other interpolators is straightforward, however, only these have been applied in the study of breaking waves.

A.2. Flux operator

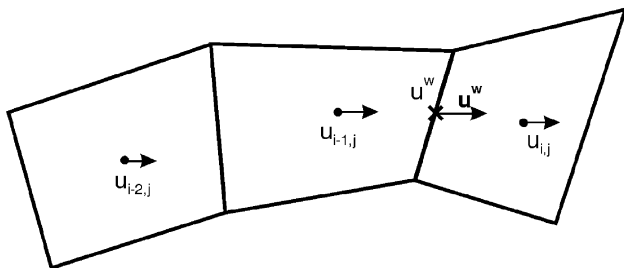
The fluxes at the eastern cell face are found by interpolation from the cell centre values to the cell face, e.g. $u_e = 1/2(u_p + u_E)$ and $w_e = 1/2(w_p + w_E)$, whereby $U^1 = u_e \cdot n_1^1 + w_e \cdot n_2^1$. The general formulation of the flux estimation is as follows:

$$U^j = I_f(u_i) \cdot n_i^j \tag{A.3}$$

where I_f denotes the interpolation operator, see above. n_i^j is the i -component ((x, y) co-ordinate system) of the area-vector of the cell face j ((ξ, η) co-ordinate system).

A.3. Gradient operators

The gradient operator, G_i , finds the gradient located at the cell centres. It is used when for instance in Eq. (15) the pressure gradient is needed for finding the tentative velocity



$$u^w = \frac{1}{2}(u_{i,j} + u_{i-1,j}) - \frac{1}{8}(u_{i-2,j} - 2u_{i-1,j} + u_{i,j})$$

CED10.05/80091-1

Fig. A.2. The convective flux of the QUICK interpolated u into the cell domain by U .

field and in Eq. (21) when the velocity field is corrected. The G_i is found as follows when it is used for internal cells flagged as FULL:

$$G_m(\phi) = \sum_l (I^l(\phi) n_m^l) \tag{A.4}$$

where I^l is the interpolation operator.

$G^j(\phi)$ is the gradient operator that gives the gradient at the cell faces. This operator is used for a part of the diffusion terms and for velocity corrections. However, this is explained in more detail in Section 2.2.1. The operator is non-orthogonal in the fluid domain except at the surface, which will be discussed later.

The gradient vector, ∇_ϕ , at the east face in two dimensions is, cf. Fig. A.3:

$$\left(\frac{\partial \phi}{\partial x} \right)_e = \left(\frac{n_1^{1e}}{\text{Vol}_e} (\phi_{i+1,j} - \phi_{i,j}) + \frac{1}{4} \frac{n_1^{2e}}{\text{Vol}_e} (\phi_{i,j+1} - \phi_{i,j-1} + \phi_{i+1,j+1} - \phi_{i+1,j-1}) \right)$$

$$\left(\frac{\partial \phi}{\partial y} \right)_e = \left(\frac{n_2^{1e}}{\text{Vol}_e} (\phi_{i+1,j} - \phi_{i,j}) + \frac{1}{4} \frac{n_2^{2e}}{\text{Vol}_e} (\phi_{i,j+1} - \phi_{i,j-1} + \phi_{i+1,j+1} - \phi_{i+1,j-1}) \right) \tag{A.5}$$

The gradients at the other faces are similar. The gradient flux operator, G^l , is found by multiplying the gradient vector by the face vector n :

$$G^l(\phi) = \nabla_\phi \cdot n_k^l \tag{A.6}$$

For the east face of the cell the gradient flux operator is:

$$\begin{aligned} G^e(\phi) &= \frac{\left(n_1^{1,e} \right)^2 + \left(n_2^{1,e} \right)^2}{\text{Vol}_e} (\phi_{i+1,j} - \phi_{i,j}) \\ &+ \frac{n_1^{2,e} \cdot n_1^{1,e} + n_2^{2,e} \cdot n_2^{1,e}}{\text{Vol}_e} \left(\frac{1}{4} \phi_{i,j+1} - \frac{1}{4} \phi_{i,j-1} \right. \\ &\left. + \frac{1}{4} \phi_{i+1,j+1} - \frac{1}{4} \phi_{i+1,j-1} \right) \end{aligned} \tag{A.7}$$

The general formulation of the gradient operator has the following form:

$$G^l(\phi) = \nabla_\phi \cdot n_k^l.$$

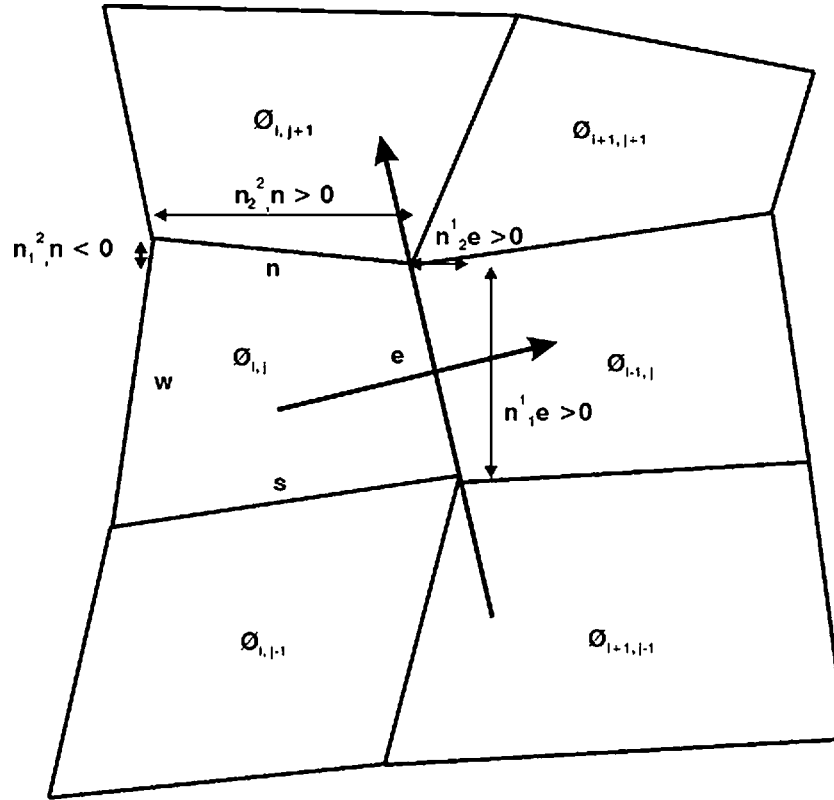
A.4. Boundary conditions

In the following the boundary conditions at the solid surfaces and at the inlet will be described. The boundary conditions at the free surface are described in the section on the free surface method.

The boundary conditions for the velocities on all the boundaries other than the free surface can be given in a very general form. Different types of boundaries can be achieved by manipulating the following equation:

$$a\phi + b \frac{\partial \phi}{\partial n} = c \tag{A.8}$$

When $a=0$ in Eq. (A.8) a Neumann condition emerges. This condition is homogeneous if $c=0$ and inhomogeneous otherwise. When $b=0$ a Dirichlet condition is obtained, and if neither a or b is equal to zero the boundary condition becomes



CED12.99/40957-9

Fig. A.3. The normal derivative is found from the value at the surface and the value in the surface cell, whereas the tangential derivative is found by extrapolation.

a Cauchy condition. On a solid boundary, if $a=0$, $b=1$, and $c=0$ the slip condition emerges.

The no-slip condition is used at the bed. In this case $a=1$ and $b=c=0$.

A.5. Surface position

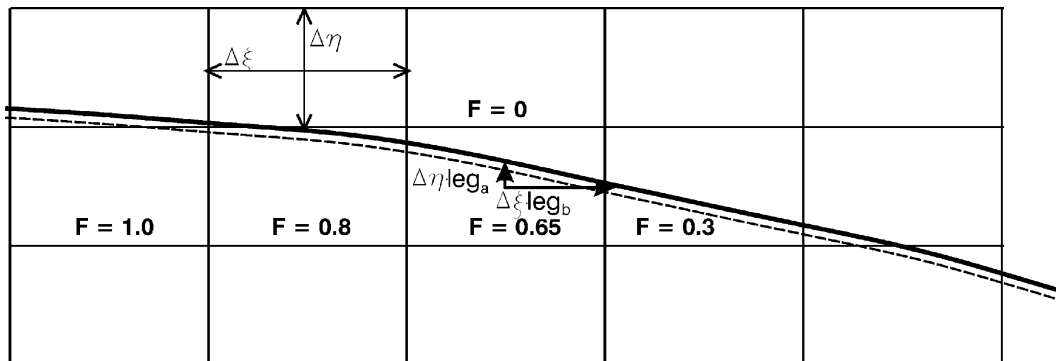
For the estimation of the pressure the exact position of the free surface has to be known. To do this it is necessary to know the state of each cell, i.e. whether the cell is a part of the fluid domain or not. Cells with F below 0.5 are flagged as VOID

cells and cells above as FULL. If a FULL cell has one or more VOID cells as neighbours the cell is reflagged as a SURFACE cell and if all neighbours are VOID as a VOID cell.

The relative distance from the surface cell centre to the surface compared to the distance from the surface cell centre to the neighbour cell centre is found as:

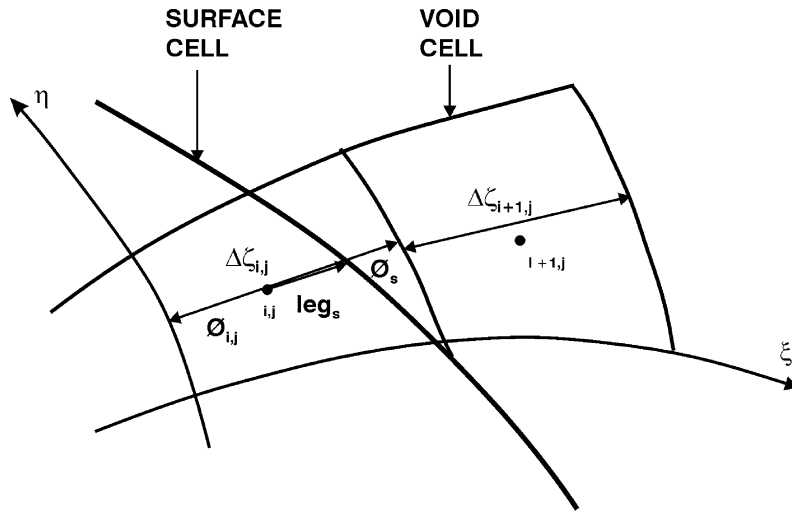
$$\text{leg}_{a,s} = F_{i,j} + F_{i,j+1} - \frac{1}{2} \tag{A.9}$$

if $\frac{\partial F}{\partial n}_{\text{Cell_face}} > \frac{\partial F}{\partial t}_{\text{Cell_face}}$, i.e. $\text{leg}_a \cdot (\partial F / \partial n)$ cell face is the gradient normal to the cell face and $\partial F / \partial t$ cell face the gradient



CED12.99/40957-5

Fig. A.4. Illustration of how the “legs” to the surface are found when the VOF-method is used. Case A: The position is found by the sum of the underlying cell contents of F , as in Eq. (A.9). Case B: The position is found by interpolation as in Eq. (A.10).



CED10.05/80091-2

Fig. A.5. The interpolation at the surface cell. First a value is extrapolated from the known values in i, j and at the surface to the VOID neighbour cell. This value is used in Eq. (A.12). From these operations the modified interpolation operator at the surface faces in Eq. (A.14) emerges.

tangential to the cell face. If the criteria are not fulfilled the following equation gives a much better approximation of the relative distance to the free surface:

$$leg_{b,s} = \frac{\left(\frac{1}{2} - F_{i,j}\right)}{(F_{i+1,j} - F_{i,j})} \quad (A.10)$$

Fig. A.4 shows two examples where Eqs. (A.9) and (A.10) apply.

A.6. Modification of the gradient operators G_i and G^j

The gradient operator G_i finds the gradient located at the cell centres. It is used when for instance the pressure gradient in Eq. (15) is used for finding the tentative velocity field and in Eq. (21) when the velocity field is corrected. The G_i is found as follows when it is used for internal cells flagged as FULL:

$$G_m(\phi) = \sum_l (I^l(\phi) \mathbf{n}_m^l) \quad (A.11)$$

where I^l is an interpolation operator as defined in Eq. (A.1).

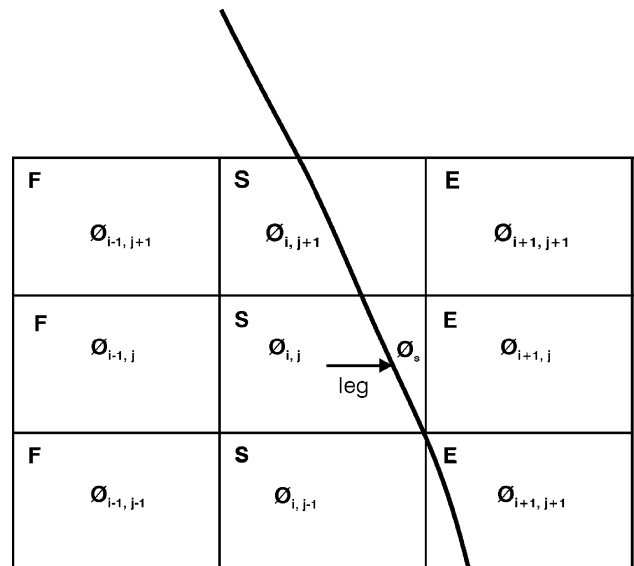
At the free surface the interpolated value cannot be found by Eq. (A.1), since the neighbour cell is not a part of the fluid domain. Instead the value at the surface, ϕ_s , is known. If a surface cell has a VOID cell to the east, the interpolation operator (A.1) has to be modified by extrapolation. Using first-order extrapolation gives (cf. Fig. A.5):

$$I^e(\phi) = \frac{1}{2} \frac{(\phi_s - \phi_{i,j})}{leg_s} + \phi_{i,j} \quad (A.12)$$

The values at a surface cell face are either found by Eqs. (A.1), (A.12) or a higher order extrapolation scheme, see

Nielsen (2003). In the following modifications made to operators refers to the 1st order extrapolation for the sake simplicity. When the modified interpolation operator is used in Eq. (A.11) the correct gradient is found in the surface cells.

The gradient operator $G^j(\phi)$ is non-orthogonal in the fluid domain except at the surface. Here it is assumed that the non-orthogonal terms are small and therefore not important to include. This introduces a minor error at the surface on non-



CED12.99/40957-8

Fig. A.6. On the non-orthogonal grid the corner, up and down values of ϕ have to be taken into account when the gradient vector, ∇_{ϕ} , is found at the cell face.

orthogonal grids, however, compared to other shortcomings at the surface these errors may be neglected.

These approximations give the x -component of the gradient for the surface position shown in Fig. A.6, where the cells (i, j) , $(i, j+1)$, $(i, j-1)$, $(i-1, j+1)$, and $(i-1, j-1)$ are FULL or SURFACE cells, as follows:

$$\frac{\partial \phi}{\partial x} = \frac{n_1^{1,e}}{\text{Vol}_e} \frac{1}{\text{leg}} (\phi_s - \phi_{i,j}) \quad (\text{A.13})$$

The gradient flux operator at the east cell face is this case modified to:

$$G^e(\phi)_{\text{surface}} = \frac{\left(n_1^{1,e}\right)^2 + \left(n_1^{1,e}\right)^2}{\text{Vol}_e} \frac{1}{\text{leg}} (\phi_s - \phi_{i,j}) \quad (\text{A.14})$$

References

- Battjes, J.A., 1988. Surf-zone dynamics. *Annu. Rev. Fluid Mech.* 20, 257–293.
- Bradford, S.F., 2000. Numerical simulation of surf zone dynamics. *J. Waterw. Port Coast. Ocean Eng.* 126 (1), 1–13.
- Chen, S., Johnson, D.B., Raad, P.E., 1991. The Surface Marker Method, Computational Modelling of Free and Moving Boundary Problems, *Fluid Flow*, vol. 1. de Gruyter, New York, pp. 226–234.
- Christensen, E.D., Deigaard, R., 2001. Large eddy simulation of breaking waves. *Coast. Eng.* 42 (1), 53–86.
- Christensen, E.D., Jensen, J.H., Mayer, S. (2000): Sediment transport under breaking waves, in Proc. of 27th Int. Conf. on Coastal Eng., ASCE, Sydney, Australia, 16–21, Vol. 3, pp 2467–2480.
- Christensen, E.D., Walstra, D.-J., Emerat, N., 2002. Vertical variation of flow across the surf zone. *Coast. Eng.* 45 (3–4), 169–198.
- Elfrink, B., Baldock, T., 2002. Hydrodynamics and sediment transport in the swash zone: a review of perspectives. *Coast. Eng.* 45 (3–4), 149–167.
- Emarat, N., Christensen, E.D., Forehand, D.I.M., Mayer, S., 2000. A study of plunging breaker mechanics by PIV measurements and a Navier–Stokes solver. Proc. of the 27th Int. Conf. on Coastal Eng., vol. 1. ASCE, Sydney, Australia, pp. 891–901.
- Ferziger, J.H., Peric, M., 1999. *Computational Methods for Fluid Dynamics*. Springer-Verlag, Berlin. 389 pp.
- Harlow, F., Welch, J., 1965. Numerical calculations of time-dependent viscous incompressible flow of fluid with free surface. *Phys. Fluids, A Fluid Dyn.* 8, 2182–2189.
- Hirt, C.W., Nichols, B.D., 1981. Volume of fluid (VOF) method for the dynamics of free boundaries. *J. Comput. Phys.* 39, 201–225.
- Jansen, P.C.M., 1986. Laboratory observations of the kinematics in the aerated region of breaking waves. *Coast. Eng.* 9 (5), 453–477.
- Kawamura, T., Miyata, H., 1994. Simulation of nonlinear ship flows by density-function method. *J. Soc. Nav. Archit. Jpn.* 176, 1–10.
- Kim, W.-W., Menon, S., 1999. An unsteady incompressible Navier–Stokes solver for large eddy simulation of turbulent flows. *Int. J. Numer. Methods Fluids* 31, 983–1017.
- Kothe, D.B., Mjolsness, R.C., Torrey, M.D., 1991. RIPPLE: A Computer Program for Incompressible Flows with Free Surfaces. Los Alamos National Laboratory, LA-12007-MS.
- Lemos, C., 1992. Wave Breaking, a Numerical Study, number 71 in *Lecture Notes in Engineering*. Springer-Verlag.
- Leonard, B.P., 1991. The ULTIMATE conservative difference scheme applied to unsteady one-dimensional advection. *Comput. Methods Appl. Mech. Eng.* 88, 17–74.
- Lin, C., Hwung, H.H., 1992. External and internal flow fields of plunging breakers. *Exp. Fluids* 12, 229–237.
- Lin, Pengzhi, Liu, Philip L.-F., 1998. A numerical study of breaking waves in the surf zone. *J. Fluid Mech.* 359, 239–264.
- Lin, Pengzhi, Liu, Philip L.-F., 1998. Turbulence transport, vorticity dynamics, and solute mixing under plunging breaking waves in surf zone. *J. Geophys. Res.* 103 (C8), 15677–15694.
- Longo, S., Petti, M., Losada, I.J., 2002. Turbulence in swash and surf zones: a review. *Coast. Eng.* 45 (3–4), 129–147.
- Mayer, S., Madsen, P.A., 2000. Simulation of breaking waves in the surf zone using a Navier–Stokes solver. Proc. 27th Int. Conf. on Coastal Eng., vol. 1. ASCE, pp. 928–941.
- Mayer, S., Garapon, A., Sørensen, L.S., 1998. A fractional step method for unsteady free-surface flow with applications to non-linear wave dynamics. *Int. J. Numer. Methods Fluids* 28 (2), 293–315.
- Menon, S., Yeung, P.-K., Kim, W.-W., 1996. Effect of subgrid models on the computed interscale energy transfer in isotropic turbulence. *Comput. Fluids* 25 (2), 165–180.
- Nadaoka, K., Kondoh, T., 1982. Laboratory measurements of velocity field structure in the surf zone by LDV. *Coast. Eng. Jpn.* 25, 125–146.
- Nadaoka, K., Ueno, S., Igarashi, T., 1988. Field observations of three-dimensional large-scale eddies and sediment suspension in the surf zone. *Coast. Eng. Jpn.* 31 (2), 277–287.
- Nadaoka, K., Hino, M., Koyano, Y., 1989. Structure of the turbulent flow field under breaking waves in the surf zone. *J. Fluid Mech.* 204, 359–387.
- Nielsen, K.B., 2003. Numerical prediction of green water loads on ships. Ph.D. thesis, Department of Mechanical Engineering, Technical University of Denmark.
- Nielsen, K.B., Mayer, S., 2004. Numerical prediction of green water incidents. *Ocean Eng.* 31, 363–399.
- Peregrine, D.H., 1983. Breaking waves on beaches. *Annu. Rev. Fluid Mech.* 15, 149–178.
- Sakai, T., Mizutani, Tanaka, H., Tada, Y., 1986. Vortex formulation in plunging breakers. Proc. 20th Int. Conf. on Coastal Eng., vol. 1. ASCE, Taipei, Taiwan, pp. 711–723.
- Smagorinsky, J., 1963. General circulation experiments with primitive equations: 1. The basic experiment. *Mon. Weather Rev.* 91, 99–164.
- Stive, M.J.F., 1980. Velocity and pressure field in spilling breakers. Proc. 17th Int. Conf. on Coastal Eng., vol. 1. ASCE, pp. 547–566.
- Stive, M.J.F., Wind, H.G., 1982. A study of radiation stress and set-up in the surf zone. *Coast. Eng.* 1, 1–25.
- Svendsen, I.A., 1987. Analysis of surf zone turbulence. *J. Geophys. Res.* 92 (C5), 5115–5124.
- Svendsen, I.A., Putrevu, U., 1996. Surf-zone hydrodynamics. In: Liu, P. L.-F. (Eds.), *Advances in Coastal and Ocean Eng.*, vol. 2, pp. 1–78.
- Ting, F.C., Kirby, J.T., 1994. Observation of undertow and turbulence in a laboratory surf zone. *Coast. Eng.* 24 (1–2), 51–80.
- Ting, F.C., Kirby, J.T., 1995. Dynamics of surf-zone turbulence in a strong plunging breaker. *Coast. Eng.* 24 (3–4), 177–204.
- Ting, F.C., Kirby, J.T., 1996. Dynamics of surf-zone turbulence in a spilling breaker. *Coast. Eng.* 27 (3–4), 131–160.
- Ubbink, O., 1997. Numerical prediction of two fluid systems with sharp interfaces, Ph.D.-Thesis, Mechanical Engineering Dept., Imperial College, University of London (1997) p. 69.
- Watanabe, Y., Saeki, H., 1999. Three-dimensional large eddy simulation of breaking waves. *Coast. Eng. J.* 41 (3 & 4), 281–301.
- Watanabe, Y., Saeki, H., 2002. Velocity field after wave breaking. *Int. J. Numer. Methods Fluids* 39, 607–637.
- Watanabe, Y., Yasuhara, Saeki, H., 2000. Three-dimensional large-scale eddies of breaking waves. Proc. 27th Int. Conf. on Coastal Eng., vol. 1. ASCE, pp. 942–951.
- Yoshizawa, A., 1986. Statistical theory for compressible turbulent shear flows with application to sub-grid modelling. *Phys. Fluids, A Fluid Dyn.* 29 (7), 2152–2164.
- Zhao, Q., Tanimoto, K., 1998. Numerical simulation of breaking waves by large eddy simulation and VOF-method. Proc. 26th Int. Conf. Coastal Eng., vol. 1. ASCE, pp. 892–905.
- Zhao, Q., Armfield, S., Tanimoto, K., 2000. A two-dimensional multi-scale turbulence model for breaking waves. Proc. 27th Int. Conf. Coastal Eng., vol. 1. ASCE, pp. 80–93.
- Zhao, Q., Armfield, S., Tanimoto, K., 2004. Numerical simulation of breaking waves by a multi-scale turbulence model. *Coast. Eng.* 51 (1), 53–80.